PHILOSOPHICAL TRANSACTIONS A

royalsocietypublishing.org/rsta

CC BY

Research

Cite this article: Hubert D *et al.* 2026 Tropospheric Ozone Assessment Report II: Past and present tropospheric ozone using satellite observations. *Phil. Trans. R. Soc. A* **384**: 20250274.
https://doi.org/10.1098/rsta.2025.0274

Received: 3 February 2026
Accepted: 13 May 2026

One contribution of 8 to a theme issue 'Tropospheric Ozone Assessment Report II'.

Subject Areas:
atmospheric science, climatology, geophysics, atmospheric chemistry

Keywords:
tropospheric ozone, atmospheric composition, satellite observations, seasonal cycle, trends, COVID-19, wildfires, TOAR-II

Author for correspondence:
Daan Hubert
e-mail: daan.hubert@aeronomie.be

Supplementary material is available online at https://doi.org/10.6084/m9.figshare.c.8658250.

THE ROYAL SOCIETY PUBLISHING

Tropospheric Ozone Assessment Report II: Past and present tropospheric ozone using satellite observations

Daan Hubert[1], Kazuyuki Miyazaki[2,3], Gaëlle Dufour[4], Elyse A. Pennington[2], Viktoria F. Sofieva[5], Carlo Arosio[6], Brice Barret[7], Anne Boynard[8,9], Melanie Coldewey-Egbers[10], Juan Cuesta[11], Klaus-Peter Heue[10], Arno Keppens[1], Natalya A. Kramarova[12], Jean-Christopher Lambert[1], Diego Loyola[10], Andrea P. Orfanoz-Cheuquelaf[6,13], Richard Siddans[14,15], Roeland Van Malderen[16,17], J. Pepijn Veefkind[18,19], Catherine Wespes[20] and Jerry R. Ziemke[21,22]

[1]Royal Belgian Institute for Space Aeronomy (BIRA-IASB), Brussels, Belgium
[2]Jet Propulsion Laboratory (JPL), California Institute of Technology, Pasadena, 91109 CA, USA
[3]Joint Institute for Regional System Science and Engineering (JIFRESSE), University of California, Los Angeles, CA, USA
[4]Université Paris Cité and Univ Paris Est Créteil, CNRS, LISA, Paris 75013, France
[5]Finnish Meteorological Institute, Helsinki, Finland
[6]Institute of Environmental Physics, University of Bremen, Bremen, Germany
[7]LAERO, Université de Toulouse-Paul Sabatier/CNRS, Toulouse, France
[8]LATMOS/IPSL, Sorbonne Université, UVSQ, CNRS, Paris, France
[9]SPASCIA, Ramonville-Saint-Agne, France
[10]Remote Sensing Technology Institute, German Aerospace Center (DLR), Oberpfaffenhofen, Germany
[11]Univ Paris Est Créteil and Université Paris Cité, CNRS, LISA, Créteil, France
[12]NASA Goddard Space Flight Center (GSFC), Greenbelt, MD, USA

© 2026 The Authors. Published by the Royal Society under the terms of the Creative Commons Attribution License http://creativecommons.org/licenses/by/4.0/, which permits unrestricted use, provided the original author and source are credited.

Downloaded from royalsocietypublishing.org/rsta/article-pdf/doi/10.1098/rsta.2025.0274/6174218/rsta.2025.0274.pdf
by German Aerospace Centre (DLR) user
on 26 October 2026

[13]Environmental Modeling, Max Planck Institute for Meteorology, Hamburg, Germany
[14]National Centre for Earth Observation and [15]Remote Sensing Group, STFC Rutherford Appleton Laboratory (RAL), Chilton, Oxfordshire, UK
[16]Royal Meteorological Institute of Belgium (KMI), Uccle, Belgium
[17]Solar-Terrestrial Centre of Excellence (STCE), Uccle, Belgium
[18]Royal Netherlands Meteorological Institute (KNMI), De Bilt, The Netherlands
[19]Delft University of Technology, Delft, The Netherlands
[20]Spectroscopy, Quantum Chemistry and Atmospheric Remote Sensing (SQUARES), Université Libre de Bruxelles (ULB), Brussels, Belgium
[21]Goddard Earth Sciences Technology and Research II (GESTAR II), Baltimore, MD, USA
[22]Morgan State University, Baltimore, MD, USA

DH, 0000-0002-4365-865X

Satellite observations enable global assessments of ozone in the free troposphere, yet uncertainties in earlier records limited the first Tropospheric Ozone Assessment Report's (TOAR-I) confidence in regional distributions and, especially, decadal trends. Here, we leverage longer and improved satellite records, additional datasets and new harmonization approaches to provide a second, more confident, TOAR assessment of present-day and longer-term changes. We quantify the 2018–2022 climatology and seasonal cycle at $1° \times 1°$ resolution and evaluate trends in a combined tropospheric column record since 2005. Summertime maxima exceed 50 DU over the Middle East, and annual-mean values exceed 40 DU from East Asia to the Mediterranean. The present-day global tropospheric ozone burden is 336 ± 6 Tg. Decadal ozone changes are pronouncedly nonlinear: increases of 2–4.5% per decade during 2005–2019 occur over 20% of the globe (high confidence), most notably across Asia, followed by widespread declines after 2020, producing a net decrease since 2005 across 70% of the globe. Dynamical and episodic drivers, such as El Niño–Southern Oscillation, extreme wildfires, and the COVID-19 pandemic, strongly influenced variability, underscoring the sensitivity of tropospheric ozone to both natural and anthropogenic influences and the critical need for sustained, coordinated satellite monitoring.

This article is part of the theme issue 'Tropospheric Ozone Assessment Report II'.

1. Introduction

Understanding and monitoring tropospheric ozone, an important pollutant and greenhouse gas, has become increasingly important owing to the widespread exceedance of air quality (AQ) standards, varying long-term trends across regions [1,2], increasing risks on human health [3] and crop yields [4] and the growing interactions between climate and air pollution [5,6]. While surface monitoring networks provide long-term data critical for trend assessment, as compiled in the first phase of the Tropospheric Ozone Assessment Report (TOAR-I) [7], their spatial coverage and long-term records are limited, especially in developing countries, over the oceans, and in the Southern Hemisphere (SH). Vertical profiles from ozonesondes, lidar and aircraft programs together with vertically integrated information from FTIR (Fourier transform infrared spectroscopy) and Dobson Umkehr instruments provide essential insights into tropospheric ozone [8–10], though their spatial and temporal sampling remains sparse. Furthermore, chemical transport and climate models continue to face challenges related to uncertainties in emissions inputs and the representation of atmospheric chemistry and physical processes [11].

Satellite remote sensing is therefore a critical component of the global ozone observing system. It provides near-global coverage and vertically integrated information on tropospheric ozone and its precursors. Instruments such as the Ozone Monitoring Instrument (OMI) onboard Aura,

Downloaded from royalsocietypublishing.org/rsta/article-pdf/doi/10.1098/rsta.2025.0274/6174218/rsta.2025.0274.pdf
by German Aerospace Centre (DLR) user
on 26 October 2026

the Global Ozone Monitoring Experiment-2 (GOME-2) onboard Metop, the Tropospheric Monitoring Instrument (TROPOMI) onboard Sentinel-5P, the Infrared Atmospheric Sounding Interferometer (IASI) onboard Metop and the Cross-track Infrared Sounder (CrIS) onboard Suomi NPP and JPSS have produced long-term ozone records, with successive sensor generations providing improved spatial and temporal sampling and coverage. More recently, geostationary missions, such as Korea's Geostationary Environment Monitoring Spectrometer (GEMS), the U.S. Tropospheric Emissions: Monitoring of Pollution (TEMPO) and Europe's Sentinel-4, have advanced atmospheric composition monitoring by enabling detailed analyses of diurnal ozone variability and the evolution of urban pollution plumes over continental scales.

To address the limitations of individual satellite products, particularly related to differences in spatio-temporal coverage and vertical sensitivity, chemical data assimilation systems that integrate satellite observations of ozone and its precursors have emerged as powerful tools to generate spatially, temporally and vertically consistent three-dimensional distributions across the troposphere [12,13]. Also, recent developments in machine learning approaches have expanded the possibilities for satellite product integration [14]. Nevertheless, the effectiveness of these approaches remains sensitive to the continuity and quality of observations, as well as model representation errors [15]. As such, rigorous evaluation of the original satellite ozone products remains essential for benchmarking, uncertainty characterization and ensuring traceability.

Addressing these satellite challenges requires coordinated community efforts to evaluate existing data products and to provide users with robust, traceable guidance. This is one of the key motivations of TOAR, an initiative of the International Global Atmospheric Chemistry project (IGAC). TOAR-I (2014–2019) provided the first systematic global assessment of ozone observations and trends at the surface and in the free troposphere [1,16]. The ongoing second phase, TOAR-II (2020–2025), extends this effort by incorporating longer timescales and additional, more mature datasets. This paper presents the TOAR-II Satellite Ozone Assessment, which includes a comprehensive harmonization, combination and evaluation (§3) of current satellite data records (§2) to infer the present-day annual mean (§4) and seasonal cycle (§5) of tropospheric ozone, as well as long-term changes (§6) and short-term disturbances caused by unusual events, including the COVID-19 lockdown and wildfires (§7), since the mid-2000s.

2. Data

(a) Satellite remote sensing

The amount of ozone in the troposphere, which represents about 10% of the total atmospheric burden, is inferred from satellite observations using three independent techniques: nadir profile (NP) retrieval, tropospheric ozone residual (TOR) and convective cloud differential (CCD). In this assessment, we focus on tropospheric column ozone (TrOC), i.e. the amount of ozone between the surface and the thermal tropopause, while acknowledging that satellite sensors have limited sensitivity to ozone near the surface and within the boundary layer. Table 1 lists the 15 satellite data records considered in this study (9× NP, 5× TOR and 1× CCD). For brevity, acronym definitions and technical details for each product are provided in §S1.1 in the supplementary material. Here, we provide a concise overview of the measurement techniques and the primary challenges affecting data quality and data comparability. Section 3a discusses how the datasets were further processed, in an attempt to resolve some of their intrinsic differences.

Nadir Profile (NP). Nadir-viewing satellite sensors collect UV or TIR spectra, from which the vertical distribution of ozone can be inferred at a vertical resolution of 5–10 km across troposphere and stratosphere. In addition to instrument noise and calibration errors in the spectral data, the retrieved profiles are influenced by factors, such as the choice of prior ozone profile and prior constraints, the spectroscopic database, the radiative transfer model and related assumptions. Ozone values, expressed as concentrations or mixing ratios, are reported at multiple vertical levels in the

Downloaded from royalsocietypublishing.org/rsta/article-pdf/doi/10.1098/rsta.2025.0274/6174218/rsta.2025.0274.pdf
by German Aerospace Centre (DLR) user
on 26 October 2026

Downloaded from royalsocietypublishing.org/rsta/article-pdf/doi/10.1098/rsta.2025.0274/6174218/rsta.2025.0274.pdf
by German Aerospace Centre (DLR) user
on 26 October 2026

Table 1. Characteristics of the 15 satellite datasets considered in this assessment, grouped by measurement technique and ordered by the start time of the data record. The second-to-last column lists which TrOC metrics (described in footnote) the data record contribute to the combined satellite estimate.

	satellite record	provider	coverage (time, horizontal)	native top level[1]	spectral domain[2]	TOAR-II combined[3]	references
NP	GOP-ECV	DLR/RAL/ESA	1996/01–2022/04, global	–	UV	M	[17,18]
	TROPOMI	KNMI/ESA	2018/10–2024/06, global	-	UV	M	[18,19]
	IASI-CDR	ULB/LATMOS/AC SAF	2008/07–2023/06, global	-	TIR	MSCE	[18,20–22]
	IASI SOFRID	LAERO	2008/07–2023/06, global	-	TIR	MSCE	[21]
	IASI KOPRA	LISA	2008/07–2023/06, USA, EUR, People's Republic of China	-	TIR	SCE	[21–23]
	IASI-GOME2-B	LISA/AERIS	2017/07–2024/06, global	-	TIR-UV	MSCE	[1,18,24]
	AIRS TROPESS	NASA JPL	2003/07–2023/06, 65° S–85° N	-	TIR	MSCE	[25,26]
	AIRS-OMI TROPESS	NASA JPL	2005/07–2023/06, 65° S–85° N	-	TIR-UV	MSCE	[25–27]
	CrIS TROPESS	NASA JPL	2016/07–2021/06, 65° S–85° N	-	TIR	SCE	[25,26]
TOR	OMI-LIMB	FMI/DLR/ESA	2005/04–2024/06, global	LRT (ERA5) & ozonopause	UV, MW, IR	MSCE	[18,28,29]
	OMI-MLS	NASA GSFC	2005/04–2024/06, 60° S–60° N	LRT (NCEP)	UV, MW	MSCE	[18,29–31]
	OMPS-LNM	IUP-UB	2012/08–2023/06, 60° S–60° N	LRT (ERA5) & 3.5 PVU	UV	MSCE	[18,29,32]
	OMPS-MERRA2	NASA GSFC	2012/07–2024/06, global	$\theta = 380$ K & 2.5 PVU	UV, reanalysis	MSCE	[18,29,33]
	EPIC-MERRA2	NASA GSFC	2015/12–2024/02, global	$\theta = 380$ K & 2.5 PVU	UV, reanalysis	MSCE	[18,33–38]
CCD	GTTO-ECV	DLR/BIRA-IASB/ESA	1996/01–2024/06, 20° S–20° N	270 hPa	UV	SCE	[18,39]

[1]LRT: lapse rate tropopause (i.e. thermal tropopause); θ: potential temperature, PVU: potential vorticity unit.
[2]UV: ultraviolet; TIR: thermal infrared; MW: microwave.
[3]M: present-day mean state; S: present-day seasonal cycle; C: long-term changes; E: episodic events.

troposphere, but the retrieved values are highly correlated. Generally, NP records provide at most one independent piece of tropospheric information, distributed through the troposphere according to the retrieval's vertical sensitivity, which in turn depends on the spectral domain. Nine NP data records are considered in this study, all but one providing single vertical profiles (L2 data). One set of records relies primarily on IR measurements by the European IASI sensors (IASI-CDR, IASI SOFRID, IASI KOPRA and IASI-GOME2-B). A second set applies the TROPESS retrieval algorithm to U.S. sensors operating mainly in the IR (AIRS, CrIS, AIRS-OMI). A third set is based solely on UV observations by European sensors (TROPOMI, GOP-ECV).

Tropospheric Ozone Residual (TOR). The TOR method infers tropospheric information by subtracting co-located total columns from a nadir-viewing sounder and stratospheric columns from a limb-viewing sensor or a reanalysis system [40,41]. This method generally leads to spatially and temporally gridded TrOC data (L3 data) between the surface and a predefined top level that is often located around the tropopause, given the large uncertainty in limb ozone profiles below the tropopause. Measurement uncertainty arises from the limited vertical resolution of limb sounders in the upper troposphere—lower stratosphere (UTLS), where ozone gradients are large, from lower signal-to-noise ratios in the UTLS region and from the weaker sensitivity of nadir sounders to near-surface ozone [28,32]. The main differences between the considered TOR records are the sources of total and stratospheric columns, the definition of the top level and the sampling resolution. Five TOR data records are used in this assessment, relying on Aura MLS (OMI-LIMB, OMI-MLS), OMPS Limb Profiler (OMPS-LNM) or the MERRA-2 reanalysis (OMPS-MERRA2, EPIC-MERRA2) to estimate the stratospheric ozone column, or on the OMI (OMI-LIMB, OMI-MLS), OMPS Nadir Mapper (OMPS-LNM, OMPS-MERRA2) or EPIC sensor (EPIC-MERRA2) for the total column.

Convective Cloud Differential (CCD). The CCD algorithm applies a residual approach, similar to the TOR method, in which TrOC is derived as the difference between total and stratospheric ozone columns [39,41]. In contrast to TOR, both columns come from the same nadir-viewing sensor but they are generally not co-located. The stratospheric column is estimated from ozone column retrieved above deep convective clouds. Assuming zonal invariance, it is then subtracted from total ozone column data over clear-sky scenes within the same latitude belt. The inherent top level of CCD column data is determined by the altitude of high convective clouds (approx. 200–300 hPa). Thus, this technique can only be applied in the tropical region, where strong convective activity occurs frequently enough and zonal invariance is approximately fulfilled. Recently, new algorithms were proposed that do not require zonal invariance and can be applied outside the tropics [42,43]. In this assessment, we use GTTO-ECV, which is based on the European series of nadir UV sensors. Other CCD datasets were not considered because they either include older data versions from a subset of the sensors already incorporated in GTTO-ECV or do not cover recent years [44,45]. CCD column uncertainties are mainly owing to zonal variations of the stratospheric column, corrections for in-cloud column amounts, loss of sensitivity to ozone near the surface and other factors.

(b) *In situ* and data assimilation

Ozonesonde. *In situ* measurements by ozonesonde have long served as the reference standard for satellite validation, providing long-term records of ozone profiles with about 150 m vertical resolution. Recent reprocessing by the working group Harmonization and Evaluation of Ground-based Instruments for Free Tropospheric Ozone Measurements (HEGIFTOM) of TOAR-II and the Southern Hemisphere ADditional OZonesondes network (SHADOZ) has reduced biases from differing equipment, operating procedures or post-processing, lowering measurement uncertainty to about 5% (5–10% in the tropics) [8,10,46]. We use this homogenized dataset as the most up-to-date validation record. While the temporal coverage varies by site, the ozonesonde record used in this study spans July 1995 to June 2024. Sites were further grouped into regions following the approach

Downloaded from royalsocietypublishing.org/rsta/article-pdf/doi/10.1098/rsta.2025.0274/6174218/rsta.2025.0274.pdf
by German Aerospace Centre (DLR) user
on 26 October 2026

described in §S1.2 in the supplementary material. A map of site locations is provided in figure S1.1 in the supplementary material, with details in table S1.1 in the supplementary material.

Chemical reanalysis. Chemical data assimilation products, such as the Copernicus Atmosphere Monitoring Service ReAnalysis (CAMSRA) [13] and the Tropospheric Chemistry Reanalysis version 2 (TCR-2) [47], provide independent, physically consistent fields for evaluating satellite observations of tropospheric ozone. By assimilating a common set of observational datasets, including tropospheric NO_2 and CO columns and Aura MLS ozone profiles above 215 hPa into both reanalyses, together with total column measurements in CAMSRA, these products provide spatio-temporally continuous ozone distributions. CAMSRA assimilates total column ozone, MLS ozone profiles and precursor species simultaneously within a physically consistent framework. As a result, it provides a more integrated estimate of tropospheric ozone than satellite products derived solely from stratospheric profiles and total column ozone, because it also accounts for the effects of transport and chemistry. Well-validated chemical reanalysis products, although still subject to some biases especially at the surface [15,48], serve as valuable references for assessing satellite retrieval biases, identifying sampling representativeness issues and providing vertical profile information. In addition, optimized precursor fields can be used to attribute observed ozone anomalies. Furthermore, well-validated satellite tropospheric ozone data can provide important constraints for further improving chemical reanalysis products [12].

3. Challenges for assessments

This section discusses the central challenges in assessing the information conveyed by multiple observational data records. We address two key questions: (i) how to post-process these datasets to obtain more directly comparable quantities, and (ii) how to synthesize results across records to derive robust conclusions.

(a) Data harmonization

Differences in the production process of satellite tropospheric ozone records (sensors, measurement technique, spectral range, retrieval assumptions, ancillary data and so on) propagate into measurement uncertainty as well as sampling- and smoothing-related errors, leading to discrepancies between datasets that can vary in space and time [18]. It is worth emphasizing that even in the absence of measurement error, datasets may still differ in their spatial patterns or trends purely because the retrieval's vertical sensitivity [23] or the sensor's sampling scheme [49] interacts differently with the natural variability and persistent gradients of tropospheric ozone. At the time of the TOAR-I report, sampling- and smoothing-related effects were not yet well characterized, and were hypothesized to contribute to TOAR-I's inconclusive assessment of long-term TrOC changes and of regional-scale patterns of the multi-annual mean TrOC [16].

Since then, new harmonization approaches have been developed targeting the differences in sampling and smoothing. A common vertical top level of the tropospheric column can now be applied consistently across datasets [18,29]. However, harmonizing the vertical smoothing of nadir profilers proves difficult [18], and sampling differences in the horizontal and temporal domains remain to be investigated. Section S3 in the supplementary material discusses the status of successive levels of harmonization in more detail (summarized in the supplementary material, table S3.1) from the satellite teams' original products (Tier 0) to regridding onto a common horizontal-temporal grid (Tier 1), adopting a common vertical top level (Tier 2) and efforts to account for the vertical smoothing of NP data (Tier 3).

Tier 2 harmonized satellite data provide the basis of this TOAR-II assessment report, as they achieve an optimal balance between minimizing known discrepancies among the satellite records and introducing uncertainty associated with imperfect harmonization methods or transfer

Downloaded from royalsocietypublishing.org/rsta/article-pdf/doi/10.1098/rsta.2025.0274/6174218/rsta.2025.0274.pdf
by German Aerospace Centre (DLR) user
on 26 October 2026

standards [18]. Tier 3 harmonization for NP records warrants further investigation and should be a key objective for future TOAR assessments. Throughout this work, tropospheric ozone data (by satellite, ozonesonde or reanalysis) were processed to represent the 1°× 1° monthly mean ozone column, integrated between the surface and the thermal tropopause, expressed in Dobson Units (1 DU = 4.46×10^{-4} mol m^{-2}). The thermal tropopause was derived from MERRA2 meteorological fields by Hoffmann & Spang [50].

(b) Combination and uncertainty estimation

A final, critical step in the assessment process is to synthesize results across different data records. This can be done in various ways and proves especially challenging when it comes to assigning uncertainty to the combined estimates. Our approach to combining satellite data aims to (a) reduce sensitivity to outliers, (b) minimize the impact of biases between datasets, (c) use an ensemble approach to infer uncertainty, and (d) provide conservative uncertainty estimates. Full methodological details for each ozone metric (present-day, seasonal cycle and long-term changes) are provided in §S4 in the supplementary material; here, we summarize the main ideas.

Objective (a) is met by using robust estimators (median and interpercentile) when combining a sample of satellite records. This reduces the need for stringent prescreening. Only clearly outlying data records are excluded upon visual inspection. The resulting dataset selection differs slightly by metric in order to include as much useful information as possible (see the second-last column in table 1). Objective (b) is addressed by combining individual satellite records in TrOC anomaly space, removing their own spatial or temporal mean prior to aggregation. Doing so essentially reduces biases between data records substantially, which improves the constraints on the combined result. Objective (c) reflects the fact that uncertainty budgets are not reported consistently across satellite products and are missing for some records. Hence, we infer the uncertainty on the combined estimates from the statistical dispersion (e.g. interpercentile) between satellite records. Objective (d) is to incorporate qualitative, conservative information about correlated uncertainty between data records. It is done by reducing the effective sample size, hereby avoiding an overly optimistic value for uncertainty on the combined estimates.

(c) Time-series analysis

Trends are estimated for each grid cell $\mathbf{x}$ from deseasonalized anomaly TrOC time series $\delta F(\mathbf{x}, t)$ using multiple linear regression and a model that includes a linear term (representing 'trend'), regressors that capture interannual variability (El Niño–Southern Oscillation (ENSO) and Quasi-Biennial Oscillation (QBO)) and a noise term

$$\delta F(\mathbf{x}, t) = \alpha(\mathbf{x}) + \beta(\mathbf{x})\, t + \gamma_1(\mathbf{x})\, \mathrm{ENSO}(t) + \gamma_2(\mathbf{x})\, \mathrm{QBO}_{30}(t) + \gamma_3(\mathbf{x})\, \mathrm{QBO}_{50}(t) + \epsilon(\mathbf{x}, t),$$

where α, β, and γ_i denote the regression coefficients. This model explicitly assumes a simple linear tendency of changes that are not attributed to ENSO or QBO. In the presence of nonlinear long-term changes, the derived linear trend estimates should be regarded as approximations, and their values will vary depending on the chosen start and end dates [51]. In this assessment report, the regression was carried out for two time periods: January 2005 to December 2019 and January 2005 to December 2022.

The impact of ENSO on tropospheric ozone is well established, especially over the Pacific Ocean [11]. Several studies reported that TrOC anomalies lag 4–5 month behind ENSO in the tropics, with smaller lags elsewhere [49,52]. While including a lag in the regression model can improve the fit at some locations, it has a limited impact on trend estimates and uncertainties overall [53]. We therefore use the ENSO predictor (MEI index) without an explicit lag in this work. The impact of QBO on TrOC can occur via stratosphere-troposphere exchanges (STE) [11,54] and is much weaker than ENSO [52]. TOR and CCD techniques derive tropospheric ozone by subtracting from

Downloaded from royalsocietypublishing.org/rsta/article-pdf/doi/10.1098/rsta.2025.0274/6174218/rsta.2025.0274.pdf
by German Aerospace Centre (DLR) user
on 26 October 2026

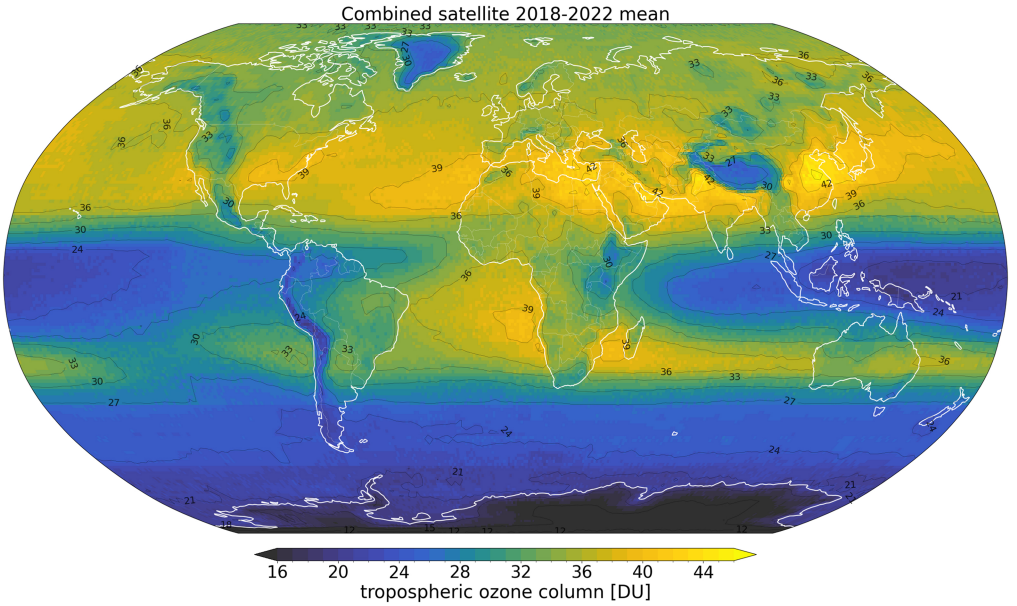


Figure 1. Present-day mean TrOC between January 2018 and December 2022 (surface to thermal tropopause, DU, 1° resolution), combining 12 satellite records. Maps for individual harmonized satellite records are shown in figure S5.2 in the supplementary material.

the total column a stratospheric component, which is strongly modulated by QBO. When the cancellation process is imperfect, an artificial QBO signal will contaminate the tropospheric ozone data [29]. For these reasons, QBO terms are included in this work (equatorial winds at 30 and 50 hPa, i.e. QBO_{30} and QBO_{50}). Across TOAR-II, some studies included QBO in their regression model [2,29,55–57] and others did not [10,49,58]. Lag-1 autocorrelation of the fit residuals ϵ is taken into account using the Cochrane–Orcutt transformation [59]. Regression coefficient uncertainties are estimated from the fit residuals [60].

4. Present-day mean state (2018–2022)

Figure S5.2 in the supplementary material shows the 2018–2022 mean spatial distribution of tropospheric ozone columns (TrOC) from 15 harmonized satellite records (§3 and [18]), corresponding to the TOAR-II reference period for present-day ozone. Two datasets (GOP-ECV and OMI-LIMB) underestimate the near-global (60° S–60° N) mean TrOC by approximately 20%; excluding them, the standard deviation of the remaining near-global mean estimates is 4%. After removing each record's 60° S–60° N mean, the spatial anomaly patterns agree very well for all 15 records across global to continental scales, with good consistency persisting down to regional scales (supplementary material, figure S5.5). All datasets show enhanced ozone in the Northern Hemisphere (NH) extratropics, lower values in the SH and over high-altitude terrain (Antarctica, Greenland, Himalayas, Andes and so on) and a zonal wave-one pattern in the tropics. The largest systematic differences occur over the polar regions (GOP-ECV, TROPOMI and OMI-LIMB), while considerable cell-to-cell variability is found in the TROPESS records (AIRS, AIRS-OMI and CrIS). Several NP products (IASI SOFRID, AIRS, AIRS-OMI and CrIS) also exhibit 5–10% discontinuities that coincide with changes in the underlying *a priori* information, underscoring the need for further harmonization of these records. Overall, these results emphasize that further improvements in calibration, retrieval and harmonization schemes will be key to improving assessments of the multi-annual mean distribution at, and below, the regional scales.

Downloaded from royalsocietypublishing.org/rsta/article-pdf/doi/10.1098/rsta.2025.0274/6174218/rsta.2025.0274.pdf
by German Aerospace Centre (DLR) user
on 26 October 2026

The (very) good overall agreement across global to regional scales supports construction of a combined satellite map (approach outlined in §3b, with details in the supplementary material, §S4.1.1), shown in figure 1. Uncertainty of combined satellite data is typically 2–5% for individual 1°× 1° grid cells (1σ), increasing to 5–15% over high-altitude terrain (supplementary material, figure S5.7, top left). Twelve satellite records were included (marked 'M' in the next-to-last column of table 1); three were excluded solely owing to more limited spatial coverage (IASI KOPRA and GTTO-ECV) or temporal coverage (CrIS), rather than data quality concerns. Figure 1 represents, to our knowledge, the first quantitative synthesis of a large and diverse suite of satellite TrOC records, accompanied by a comprehensive uncertainty analysis (supplementary material, figure S5.7). Because satellite retrievals have limited sensitivity to the boundary layer, they mainly map patterns in free-tropospheric ozone.

Figure 1 shows that 2018–2022 mean ozone levels larger than 33 DU prevail across the entire NH extratropics, with values exceeding 39 DU in the subtropical belt. The highest multi-annual mean TrOC values (>42 DU) occur over the eastern Mediterranean-northern Egypt, the Iraq-Persian Gulf region, Punjab and the eastern Indo-Gangetic Plain (IGP), the East China Sea, the Korean Peninsula and especially central-eastern China (North China Plain (NCP), Yangtze River Delta, Twain-Hu Basin and Sichuan Basin) where the global maximum reaches 46.1 ± 2.2 DU (50% above the global mean of 30.8 ± 0.6 DU). In the SH, elevated TrOC occurs over the Atlantic and the Mozambique Channel (34–40 DU) and across the subtropical belt (33–37 DU), but it remains substantially lower than the NH hot spots. By contrast, low ozone levels (20–26 DU) are found over the Southern Oceans and the tropical Pacific and Indian Oceans. Together with the Atlantic maximum, the Pacific minimum produces the tropical zonal wave-one structure. TrOC levels also clearly decrease over high-altitude terrain, with particularly low values over Antarctica, where the global minimum reaches 10.2 ± 1.5 DU (66% below the global mean).

The spatial distribution in figure 1 is in good agreement with recent and past observation-based reports [2,20,23,29,61,62], including the first TOAR assessment [1,16]. Detailed quantitative comparison is, however, hindered by differences in, for example, horizontal resolution, the analysed time periods and vertical top level, and by the emphasis in many studies on seasonal rather than annual-mean patterns. Moreover, most, if not all, multi-record studies to date report the range of ozone estimates across datasets [2,16,29] rather than combining them, as attempted here. Comparisons of 2018–2022 mean TrOC from each satellite, reanalysis and ozonesonde dataset are presented in §S9.1 in the supplementary material. Only satellite and reanalysis data that are coincident in space and time with the sonde data are used. Consistent with figure 1, TrOC tends to be highest across the NH and lowest in the tropics for each measurement technique, with eastern South America displaying higher TrOC than other locations across the tropics. The normalized mean bias (NMB) of the satellite and reanalysis dataset relative to the ozonesonde data generally falls within ±20%. Most of OMI-MLS values fall within ±10%, and likewise for IASI and TROPESS except at the NH high latitudes where these instruments provide less data. The TCR-2 and CAMS-RA reanalyses show positive NMB in all regions. Standard errors for the 2018–2022 NMB are generally smaller than the corresponding NMB values, indicating limited dispersion of regional-mean biases around their mean.

The 2018–2022 mean TrOC distribution bears the imprints of the main drivers of tropospheric ozone levels (see reviews by, e.g. Monks *et al.* [63] and Archibald *et al.* [64]): photochemical production over regions with, or downwind of, high precursor emissions (combustion, industry, lightning, biomass burning, vegetation and soil) and conducive meteorological conditions (heat extremes and solar radiation), horizontal transport between continents, convective transport between boundary layer and upper troposphere and exchanges between stratosphere and troposphere, as well as variations in tropospheric depth owing to orography and tropopause altitude. Many of these processes exhibit clear seasonal variation (§5).

The global tropospheric ozone burden (90° S–90° N) is estimated at 336 ± 6 Tg for 2018–2022, which is virtually identical to the TOAR-I estimate 339 ± 8 Tg for 2010–2014 that was based on just two satellite records [16]. Similar values are also found for the near-global burden (60° S–60° N),

Downloaded from royalsocietypublishing.org/rsta/article-pdf/doi/10.1098/rsta.2025.0274/6174218/rsta.2025.0274.pdf
by German Aerospace Centre (DLR) user
on 26 October 2026

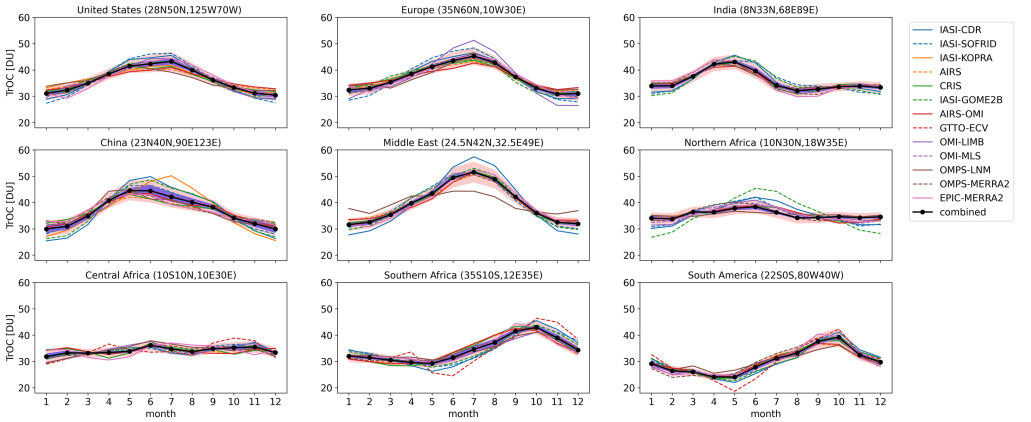


Figure 2. Seasonal cycle of present-day TrOC (2018–2022, in DU) over nine regions (defined in the supplementary material, table S2.1), for 13 satellite records (coloured) and the combined satellite estimate (black). Two methods to estimate uncertainty are compared (supplementary material, §S4.2.2): error propagation (red) and ensemble spread (blue). All individual seasonal cycles are offset to their 2018–2022 annual mean for ease of comparison. The supplementary material includes a figure without this offset (supplementary material, figure S6.5).

covered by more TOAR-I datasets: 297 ± 6 Tg for 2018–2022 (this work, 12 satellite records) versus 301 ± 8 Tg for 2010–2014 (TOAR-I, 5 satellite records). Our calculation of ozone burden and its uncertainty is detailed in §S4.1.2 in the supplementary material. Quoted intervals represent 68% confidence (1σ). Relative to TOAR-I, our estimates draw on a larger set of satellite records and apply a more complete treatment of uncertainty, resulting in more robust and tighter constraints on the global burden (1.9% versus 2.5%).

5. Present-day seasonal cycle (2018–2022)

About 12–13 satellite datasets out of 15 total (marked 'S' in the next-to-last column of table 1) display reasonably good agreement in the time of maximum, the amplitude of the seasonal cycle and their spatial structure (supplementary material, figures S6.1 and S6.2). This consistency motivates the combination of satellite information (§3b; supplementary material, §S4.2) to form near-global maps of 2018–2022 mean TrOC at monthly resolution, improving on the seasonal resolution achieved for TOAR-I (supplementary material, figures S6.3 and S6.4). This combined satellite seasonal cycle forms the basis of our assessment.

Figure 2 shows the seasonal cycle of regionally aggregated TrOC (method in the supplementary material, §S4.2.2) from all individual and the combined satellite records. In figure 2, each cycle was offset to match the 2018–2022 annual mean of the combined satellite cycle, in order to focus the comparison on the temporal structure rather than biases in the multi-annual mean level. By contrast, figure S6.5 in the supplementary material was created without this offset. Overall, the satellite records show excellent agreement on both the month of maximum TrOC and the seasonal amplitude across regions, regardless of whether the seasonal cycle is relatively weak (e.g. northern Africa) or strong (e.g. Middle East). For some regions, a subset of records is out of the conservative uncertainty estimate (red in figure 2) in terms of amplitude, but without any systematic disagreement for one record. The typical uncertainty on the combined estimate is 3–10%, increasing to as much as 20% at the SH highest latitudes (supplementary material, figure S6.4).

Further corroborating the quality of the combined satellite estimate is its excellent agreement with ozonesonde data in selected regions (supplementary material, figure S6.6). To reduce the impact of sampling differences in this comparison, a combined spatially aggregated satellite cycle was formed only using satellite data during months and in grid cells that contain sonde

Downloaded from royalsocietypublishing.org/rsta/article-pdf/doi/10.1098/rsta.2025.0274/6174218/rsta.2025.0274.pdf
by German Aerospace Centre (DLR) user
on 26 October 2026

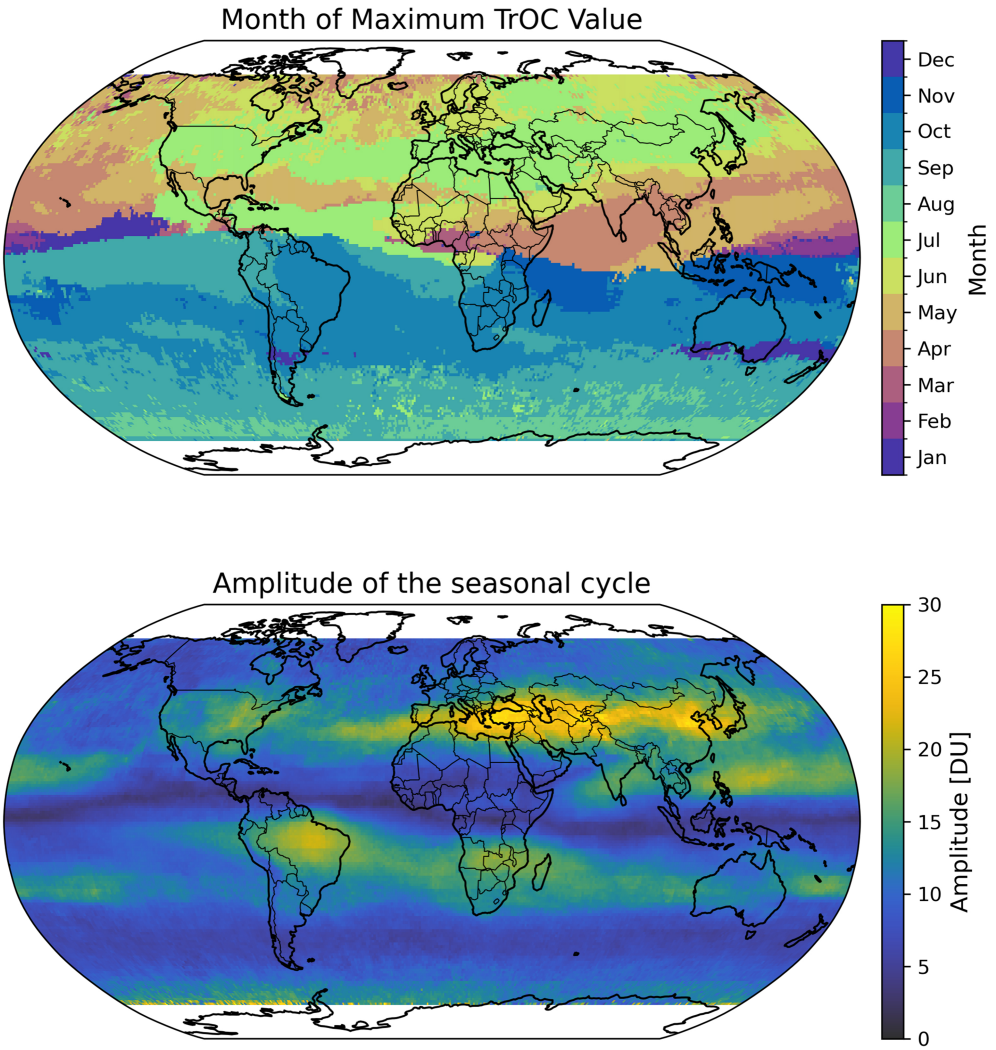


Figure 3. Month of maximum and amplitude (in DU) of seasonal cycle in present-day TrOC (2018–2022), combining information from 13 satellite records (figure 2). Only results between 70° S and 70° N are shown; outside this range the confidence in seasonal cycle estimates is lower owing to incomplete sampling (UV sensors) or lower data quality (IR sensors) during polar winter.

measurements. Figure S6.6 in the supplementary material shows that the temporal structure (correlation coefficient >95%), time of maximum and amplitude (<10%) are in a good agreement, especially in regions with dense ozonesonde coverage (Europe, tropics and northern mid-latitudes). NMB (2–7%, mostly positive) and the 1σ dispersion (2–7%) in the sonde comparison remain below the uncertainty of the combined and spatially aggregated product (6–9%). In comparison, the agreement between sondes and individual satellite is much more variable with NMB mostly falling within ±20% (supplementary material, figure S9.2) and up to a factor of two of difference for the amplitude (supplementary material, figure S9.3). This highlights the added value of the combined seasonal estimate and provides high confidence in its ability to reproduce the ozone seasonal cycle.

The combined satellite estimate shows a strong seasonal cycle for both hemispheres (figure 2; supplementary material, figure S6.3). Figure 3 shows that TrOC reaches its maximum in July, predominantly across the NH mid-latitudes from North America to East Asia. The

Downloaded from royalsocietypublishing.org/rsta/article-pdf/doi/10.1098/rsta.2025.0274/6174218/rsta.2025.0274.pdf
by German Aerospace Centre (DLR) user
on 26 October 2026

seasonal amplitude is largest within this latitude band, ranging from 15 to 30 DU. A broad summer maximum is observed over the USA, Europe, People's Republic of China and the Middle East, with the Middle East exhibiting the highest TrOC values (figure 2). This broad summer maximum has been consistently reported in previous studies, with suggested drivers including anthropogenic precursor emissions and STE [63,65]. In contrast to the summertime maximum (May–July) identified in our TrOC analysis, surface measurements in southern China reveal a peak in October [66]. IASI-KOPRA 0–6 km column data also indicate a secondary maximum in autumn across much of People's Republic of China [67], which might explain the gradual reductions until October and the seemingly small secondary peak in September in our seasonal plots for People's Republic of China.

The timing of the TrOC maximum exhibits a clear latitudinal dependence, occurring in June at most of the NH (>30° N) and shifting to May and April towards tropical NH latitudes (<30° N) across southeastern Asia, the Pacific, India and the Indian Ocean (figures 2 and 3). These features may be related to the Asian Summer Monsoon, which transports cleaner air masses from the tropical Pacific and Indian Ocean, leading to an earlier decrease in ozone over these regions [68–70]. In the NH high latitudes, the seasonal cycle is generally weak, with large uncertainties during the winter months (supplementary material, figures S6.3 and S6.4). While no clear features emerge in the mean present-day seasonal cycle, individual extreme events and corresponding seasonal changes are evident in the satellite records (§7), such as poleward transport of wildfire smoke [71].

The combined monthly product provides a unique opportunity to explore the regional patterns of ozone, which could not be resolved in TOAR-I. Focusing on the region extending from Europe to East Asia (supplementary material, figure S6.7), we find that TrOC begins to increase in early spring over East Asia, mainly in the NCP and in the IGP. TrOC reaches up to 60 DU in July over the NCP and 57 DU in June and July in the northwestern IGP. The region of high TrOC levels extends westward into Central Asia, the Middle East and the Eastern Mediterranean in June, reaching its maximum in July with TrOC values ranging from 51 to 57 DU across a broad region spanning from the Western Mediterranean to Central Asia. This extended maximum likely reflects a combination of ozone production from local precursor emissions, transport from Europe to the Mediterranean, large occurrence of STE events in the eastern Mediterranean region in summer and subsidence of UTLS air masses, enriched in ozone, in particular in summer by upward advection and transport of ozone-rich air masses from Asia by the Asian summer monsoon circulation [72–74]. Downward transport is also linked to tropopause folds [75,76], with the Eastern Mediterranean and Central Asia most sensitive to shallow folds [77]. TrOC progressively decreases to its minimum in November-December in this Eurasian region and more generally in the NH (supplementary material, figure S6.7).

Turning to the North Atlantic (supplementary material, figure S6.8), we find that, in the western part, TrOC starts to increase in April (not shown) in the southeast of the USA. The region of high TrOC levels extends then to Central USA and the east coast to reach maxima of about 50 DU at the north of the east coast in July, after which the enhanced ozone is transported eastward over the Atlantic [78,79]. In the eastern North Atlantic, an ozone plume is visible westward to the African coasts southward of 32° N in April and moving northward between 30° N and 40° N in summer months. Studies at the Izaña GAW observatory reported ozone maximum in spring-early summer in the subtropical North Atlantic resulting from long range transport from North America, ozone production during transport and STE processes, driven by deep lows and cut-off lows west of the Iberian Peninsula [80,81]. The combined product shows then an ozone belt over the North Atlantic with TrOC values ranging from 45 to 50 DU (supplementary material, figure S6.8).

In the SH, TrOC starts to increase markedly in September across the South Atlantic Ocean, central/southern Africa and Amazonia, reaching a maximum in October with values exceeding 45 DU (supplementary material, figure S6.3; figure 2). The upper tropospheric ozone is strongly influenced by lightning NO_x in this region (e.g. [62,82,83]) with the largest contribution over the Atlantic during the December-January-February and March-April-May seasons [82]. The September-October maximum identified here likely reflects the combined influence of lightning NO_x, biomass

Downloaded from royalsocietypublishing.org/rsta/article-pdf/doi/10.1098/rsta.2025.0274/6174218/rsta.2025.0274.pdf
by German Aerospace Centre (DLR) user
on 26 October 2026

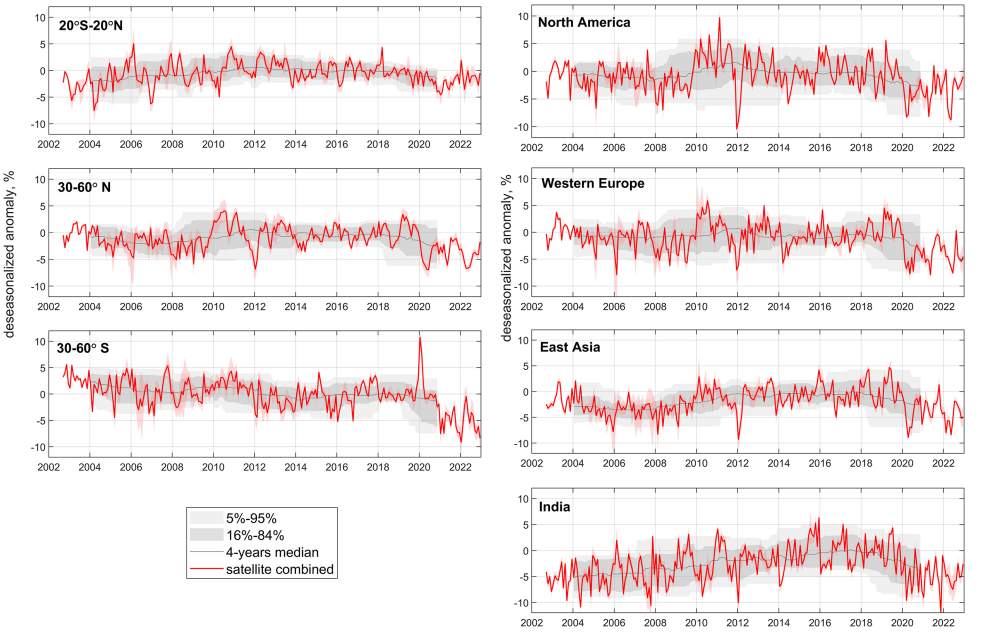


Figure 4. Time series of relative deseasonalized TrOC anomalies (in %, red), combining 13 satellite records over three latitude belts and four regional domains (defined in the supplementary material, table S2.1). The longer term evolution and interannual variability are visualized by the median (grey line), the 16th–84th (dark grey) and 5th–95th (light grey) percentile ranges in 4-year moving windows. Anomalies were offset to zero mean over 2015–2019 to highlight the impact of the COVID-19 pandemic (§7). Figure S7.4 in the supplementary material shows anomalies with ENSO and QBO signals removed.

burning maximum which also coincide with a maximum in the stratosphere-to-troposphere transport, e.g. [10,16,84]. In the SH mid-latitudes, the ozone maximum occurs in September (supplementary material, figure S6.3), but with substantially smaller TrOC values (below 30 DU) than in the NH.

6. Long-term ozone changes

Deseasonalized relative TrOC anomalies were computed for 13 satellite records (marked 'C' in the next-to-last column of table 1) using each record's own 2018–2022 climatology, then combined into four groups with quasi-independent observations (TROPESS, IASI, TOR and CCD). We find very good agreement of the grouped anomalies from monthly to annual timescales, and good agreement at longer timescales (supplementary material, figures S7.1 and S7.2). The most notable discrepancies occur for the TOR group (more negative anomalies in the extratropics prior to 2014) and for the tropical CCD record (larger variability). The four groups were subsequently combined to form a final TrOC anomaly time series (full method described in the supplementary material, §S4.3). This combined record relies on monthly data by 13 satellite records, providing a substantial advance beyond the single-satellite, annually averaged data employed in TOAR-I. More importantly, the consistency among current satellite records is markedly improved relative to the satellite data evaluated in TOAR-I [16]. We first discuss the anomaly time series (§6a) and then derived trends (§6b).

(a) Variability across timescales

Figure 4 displays deseasonalized TrOC anomalies (in %), offset to zero mean over 2015–2019, for three broad latitude bands (tropics: 20° S–20° N; NH mid-latitudes: 30° N–60° N; SH mid-latitudes:

Downloaded from royalsocietypublishing.org/rsta/article-pdf/doi/10.1098/rsta.2025.0274/6174218/rsta.2025.0274.pdf
by German Aerospace Centre (DLR) user
on 26 October 2026

30° S–60°S) and four regional domains (additional regions are shown in the supplementary material, figure S7.3). In line with previous studies [8,10,16,81,85], we observe pronounced interannual variability superimposed on longer-term, location-dependent nonlinear changes (grey line). Less than 2–4% of the observed variance in TrOC anomalies is attributed to ENSO or QBO, except over the Pacific and South East Asia where ENSO is responsible for 10–50% of TrOC variability (supplementary material, figures S7.11 and S7.4).

Characteristics of interannual TrOC variability differ between the tropics and the mid-latitudes, although certain common patterns are evident. Across all regions, a 2–4% positive anomaly occurred in 2010 (confined to the latter half of the year in the NH mid-latitudes), followed by a 6% decline during late 2011 and early 2012 (figure 4). Furthermore, a highly consistent post-2020 decrease in TrOC is seen across all satellite groups (supplementary material, figure S7.1), with mean reductions of up to 8% in the mid-latitudes and up to 4% in the tropics, linked to the COVID-19 pandemic (§7).

Among major polluted regions in the NH mid-latitudes, several common interannual features are apparent. The low ozone levels in January 2006, with pronounced reductions over Western Europe and East Asia, may partly reflect changes in transport patterns [86], although the underlying mechanisms remain uncertain. A marked NH-wide increase in 2010 (figure 4; supplementary material, figure S7.3) has been suggested to be partly linked to rising Chinese emissions [87]; however, changes in transport and other factors may also have contributed. A sharp decline in early 2012 is also consistently observed across the NH. Reduced downward transport of ozone from the stratosphere may explain part of the post-2012 decreases in the mid-troposphere and lower stratosphere [88], although further investigation is needed, and additional drivers, such as changes in precursor emissions from both anthropogenic and natural sources, as well as regional meteorological conditions, may have played important roles. The 2015–2016 period exhibits pronounced regional-scale variability (supplementary material, figure S8.1b), likely associated with the strong El Niño event, but discrepancies among satellite products remain substantial. A modest increase is apparent in 2019, followed by a decline of up to 7% during 2020–2022.

In People's Republic of China, although precursor emissions such as NO_x and CO declined, surface ozone concentrations generally increased between 2013 and 2019, with both meteorological variability and anthropogenic emissions contributing to the growth during the warmer seasons [89,90]. The combined satellite time series suggest a similar increase in the free troposphere of about 2% over the same period. By contrast, India experienced a continued ozone rise of about 5% from 2003 to 2018, likely driven by sustained growth in precursor emissions [62,91], while also exhibiting larger seasonal variations associated with the Asian monsoon. Although both countries display a relatively steady long-term increase before 2020, the underlying drivers, including changes in chemical regimes, meteorological variability and biomass burning, differ substantially [92].

In the tropics, TrOC increased from 2003 to around 2012, with short-term negative anomalies of up to 7% during the boreal spring 2004 and positive anomalies of about 5% during January–February 2006. The substantial variability in 2006 was associated with an El Niño event [93], whereas the 2010 increase has been linked to a strong La Niña [94]. From 2012 to early 2020, tropical-mean TrOC remained nearly constant, although pronounced regional-scale differences persisted. Large fluctuations were evident at smaller spatial scales. For example, in January 2012 (supplementary material, figure S8.1a), a typical La Niña pattern appeared, with decreases over the Maritime Continent and concurrent increases over the central-eastern Pacific [95]. The 2015 El Niño coincided with one of the most extreme biomass burning events over the Maritime Continent; we find increases of 25–40% in that region and 20–25% decreases over the tropical central Pacific (supplementary material, figure S8.1b), yielding a relatively small tropical-mean anomaly. In October 2019 (supplementary material, figure S8.1c), large-scale fires occurred in the Amazon and Indonesia [96], while record-breaking rainfall in Africa, associated with one of the most intense Indian Ocean Dipole events, likely suppressed ozone production [38,97]. By contrast, ozone increased over the tropical Pacific, producing pronounced zonal contrasts across the tropics.

Downloaded from royalsocietypublishing.org/rsta/article-pdf/doi/10.1098/rsta.2025.0274/6174218/rsta.2025.0274.pdf
by German Aerospace Centre (DLR) user
on 26 October 2026

ENSO modulates multiple drivers of ozone variability, including biomass burning and lightning-produced NO_x in the tropics, as well as stratospheric intrusions in the subtropics [98]. The relative importance of these mechanisms appears to vary substantially across events. A reduction of up to 4.5% was observed in 2020–2021.

In the SH mid-latitudes, TrOC during 2005–2006 was approximately 4–7% higher than in 2021–2022. An exceptional anomaly occurred around early 2020. TrOC began to increase in November 2019, and by January 2020, large positive anomalies exceeding 10% were observed, with enhanced ozone across broad areas of the SH mid- and high latitudes (§7; supplementary material, figure S8.2). This widespread rapid increase likely reflects the combined effects of multiple processes. Ozone had already begun to increase in the months preceding the peak of the 2019–2020 Australian fires, possibly influenced by Indonesian fire activity. The December 2019–January 2020 enhancement may therefore include contributions from both Indonesian and Australian wildfire emissions. Large-scale dynamical variability may also have contributed. In addition, SH winter sudden stratospheric warming events, including the late 2019 event, can enhance UTLS ozone through downward and equatorward transport of ozone-rich polar air [99,100]. Such dynamical transport, together with photochemical ozone production from wildfire emissions, has been shown to increase tropopause-level ozone by up to 30 ppb, with transport as the dominant contributor [101]. This mechanism may explain a substantial fraction of the enhanced ozone over broad regions of the SH mid- and high latitudes. The 7% decline in mid-latitude SH TrOC during January–February 2021 may be related to enhanced stratospheric ozone depletion that developed during the previous winter [102]. Substantial SH TrOC variability is also evident in early 2022 in most products. Zonal-mean ozone already started to decrease several months before the January 2022 Hunga Tonga eruption, reflecting regional-scale anomalies over areas such as Southeast Asia, the Pacific and the Amazon during the transition towards La Niña conditions (supplementary material, figure S8.4). While the Hunga Tonga eruption may have further influenced these variations through changes in stratospheric ozone, circulation and radiation [103,104], the relative contributions of these processes, including the influence of La Niña, remain uncertain and require further investigation.

(b) Long-term changes and trends

Figure 5 shows global maps of 5°× 5° resolved tropospheric ozone trends since January 2005 estimated from the combined satellite record for two end dates: December 2019 (top panel) and December 2022 (bottom panel), revealing distinct spatial patterns as well as a striking shift in trend between both periods. Estimates in different units (supplementary material, figure S7.13) or derived from zonal mean combined data (supplementary material, figure S7.15) can be found in the supplementary material. Trends derived from records with differing temporal and spatial coverage are not necessarily directly comparable. With this caveat in mind, we note that TROPESS and IASI trends are generally more consistent with the combined satellite record than those from the other two groups. TOR-group trends are systematically more positive, while CCD trends are often more negative, though more positive at some locations (supplementary material, figures S7.7 and S7.8). The standard deviation between the four groups is 1–1.5% per decade, closely matching the trend uncertainty for the combined satellite record (supplementary material, figure S7.9) obtained independently, from the regression residuals. As a result, we find high to very high confidence in trend values larger than approximately 2–3% per decade. TOAR-II calibrated language is adopted here to discuss confidence in non-zero trends (definitions in table 2 based on [53], with corresponding maps in supplementary material, figure S7.10), and we quote 1σ uncertainties unless specified otherwise.

While near-global mean levels (60° S–60° N) have increased between 2005 and 2019 ($+1.0 \pm 0.4\%$ per decade, high confidence), an overall decline since 2005 is found when the record is extended through 2022 ($-0.6 \pm 0.5\%$ per decade, low confidence). Trends shifted on average by −1.5% per decade owing to the sustained drop in TrOC during 2020–2022, with changes of (at

Downloaded from royalsocietypublishing.org/rsta/article-pdf/doi/10.1098/rsta.2025.0274/6174218/rsta.2025.0274.pdf
by German Aerospace Centre (DLR) user
on 26 October 2026

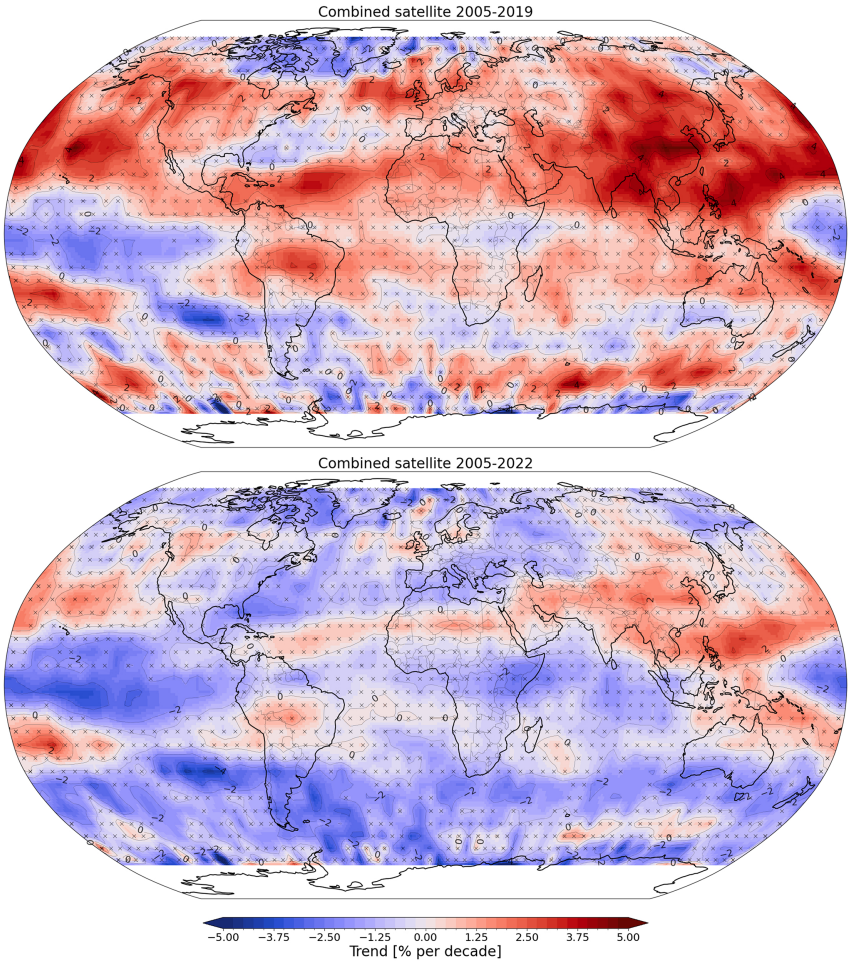


Figure 5. TrOC trend (in % per decade) between January 2005 and December 2019 (top) or January 2005 and December 2022 (bottom), inferred by multiple linear regression from deseasonalized anomaly time series combining 13 satellite records (contours every 1% per decade). Results with very low to medium confidence are stippled ($p > 0.05$). Trend maps for each of the four satellite groups can be found in §S7.3 in the supplementary material.

Table 2. Fraction of 70° S–80° N surface area with negative ($\beta < 0$) or positive trends ($\beta \geq 0$) for each period, classified following TOAR-II calibrated confidence language [53]. Corresponding trend confidence maps can be found in figure S7.10 in the supplementary material. About 4% of Earth's surface is not included in this trend assessment.

trend		signal-to-noise	2005–2019		2005–2022	
confidence	p-value	ratio $\lvert\beta/\sigma_\beta\rvert$	$\beta < 0$	$\beta \geq 0$	$\beta < 0$	$\beta \geq 0$
very high	$p \leq 0.01$	SNR ≥ 3	0%	10%	7%	0%
high	$0.01 < p \leq 0.05$	$2 \leq$ SNR < 3	2%	12%	13%	3%
medium	$0.05 < p \leq 0.10$	$1.65 \leq$ SNR < 2	2%	6%	7%	2%
low	$0.10 < p \leq 0.33$	$1 \leq$ SNR < 1.65	6%	16%	18%	6%
very low	$p > 0.33$	SNR < 1	18%	28%	26%	18%
			28%	72%	71%	29%

Downloaded from royalsocietypublishing.org/rsta/article-pdf/doi/10.1098/rsta.2025.0274/6174218/rsta.2025.0274.pdf
by German Aerospace Centre (DLR) user
on 26 October 2026

least) −2.5% per decade over India, southern and eastern China, Mongolia, Japan, the extratropical North Pacific and across the 40–60° S zonal belt (supplementary material, figure S7.12). Since a linear trend fails to describe the observed evolution during 2005–2022 at many locations, this period is not discussed in further detail, and results are shown merely to facilitate comparison to recent studies that include the COVID-19 pandemic period [8,10,20,23,29,57,58]. We leave it to future assessments, using longer combined time series, to determine whether tropospheric ozone rebounds to pre-2020 levels (as reported by Ziemke *et al.* [38]) and whether its longer-term evolution resumes the 2005–2019 trajectory.

The largest positive 2005–2019 trends (figure 5, top), +2–4% per decade (very high confidence) occurred over a vast region spanning Central Siberia to South Asia and the extratropical North Pacific. Slightly slower increases, +2–3% per decade, are observed along the zonal belt from the Middle East to the Caribbean, over northern Europe and western Canada (very high confidence) and over Brazil and the extratropical South Pacific (high confidence). The central equatorial Pacific and eastern South Pacific are the only regions where TrOC levels declined with high confidence (−2–3% per decade). Negative trends around Greenland and the Canadian Arctic (up to −2% per decade) have low confidence but are noteworthy since they are also noted in recent ground-based studies [8,10]. In summary, for the period 2005–2019, we find (high confidence) increasing tropospheric ozone levels over a fifth of the globe and decreases over a region roughly 10 times smaller (table 2). Estimates with medium to very low confidence are positive over half of the globe and negative over about 25%.

The combined satellite estimates presented here corroborate the main spatial patterns and the sign of trends collectively observed by the TOAR-II community [2,8,10,20,23,29,38,56–58,62,105–108]. Verifying quantitative agreement is more cumbersome because of the shorter length of the satellite records (generally 15–20 years) and because more than half of these studies end during the COVID-19 period at various endpoints, hereby adding noise to the trend comparison. As stated before, global mean tropospheric ozone levels have increased between 2005 and 2019. Zonal mean trends (supplementary material, figure S7.15, left) are +1.5–2% per decade over a broad 10° N–60° N zone (high confidence, equivalent to approx. 1 ppb per decade) and +0–1% per decade elsewhere (low confidence, 0–0.5 ppb per decade). There is very high confidence in tropospheric ozone increases over large parts of Asia (regional mean of about +3% per decade), while positive regional trends over Europe and the USA have low confidence (about +1% per decade).

Previous studies based on *in situ* observations have shown that variability in anthropogenic precursor emissions contributed to a broad increase in ozone across the NH during 1994–2016, despite substantial reductions in NO_x emissions at mid-latitudes [105,109–111]. By contrast, increases in tropospheric ozone from the early 2000s to the mid-2010s over tropical and subtropical regions appear to have been primarily driven by rising anthropogenic precursor emissions, in combination with favourable photochemical conditions [10,111–113]. These increases were particularly pronounced over East and South Asia, Southeast Asia, the Persian Gulf and parts of the tropics. Recent results from the HEGIFTOM working group in TOAR-II [8,10] confirm continued ozone growth across Asia and portions of the tropics, whereas North America and Europe exhibit weak positive trends or slight declines, reflecting the combined influences of emission controls, climate variability and long-range transport.

7. Episodic events: COVID-19 pandemic and wildfires

The combined satellite anomaly data capture short-term changes in TrOC associated with episodic events caused, for example, by large wildfires or drastic changes in human activities. During the COVID-19 pandemic in 2020, unprecedented reductions in anthropogenic emissions led to substantial decreases in tropospheric ozone. A sharp decline is seen across most satellite datasets in 2020, with persistently low levels extending into 2021 and 2022 (supplementary material, figure S8.3). In the combined data, the reduction is strongest in spring and early summer,

Downloaded from royalsocietypublishing.org/rsta/article-pdf/doi/10.1098/rsta.2025.0274/6174218/rsta.2025.0274.pdf
by German Aerospace Centre (DLR) user
on 26 October 2026

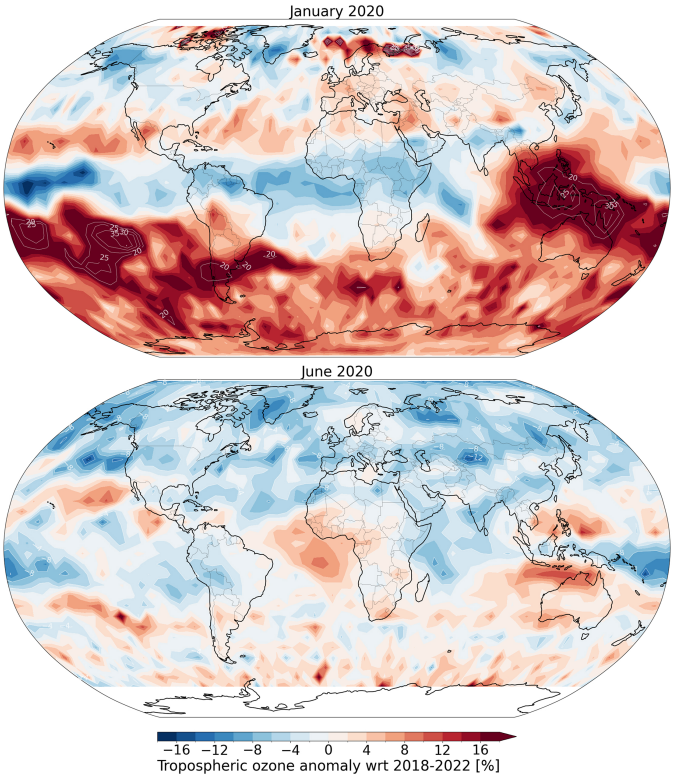


Figure 6. Deseasonalized TrOC anomaly relative to 2018–2022 seasonal cycle from the combined satellite record during January 2020 (top; Australian wildfires) and June 2020 (bottom; COVID-19 pandemic).

reaching −7% in 2020 and 2022 and −6% in 2021 in the NH extratropics (figure 4). Similar reductions over the NH mid-latitudes in 2020 have been reported using individual satellite products [33,114], ozonesondes, lidars and commercial aircraft data [115,116], as well as chemical reanalyses [117]. These studies generally attribute the observed decreases to reductions in precursor emissions and anomalous downward transport from the stratosphere [38,117]. In the SH extratropics, ozone reductions reached −7% during late 2020 and the summer season, with a similar feature observed again in late 2022. Spatial distributions (figure 6, bottom; supplementary material, figure S8.3) indicate widespread decreases across the NH mid- and high latitudes, accompanied by strong variability from late 2021 to early 2022 when a recovery from the decline occurred. The variability in the tropics also shows a slight negative tendency, consistent with ozonesonde results [57]. Near-global (60° S–60° N) annual mean TrOC levels were approximately 3% smaller in 2021–2022 than during 2015–2019. A future extension of the combined satellite record may confirm recent reports of a return to pre-pandemic levels in 2024 [38].

Another key short-term feature detected by the combined satellite data is the impact of wildfire events. In January 2020 (figure 6, top), TrOC anomalies exceeded 20% over the Maritime Continent and Australia, with enhancements extending into the SH subtropical Pacific along the westerly jet. Moderate increases also extended to the SH high latitudes, although these were accompanied by localized reductions of 5–10%. Analyses from IASI indicate that the Australia wildfires caused drastic increases in several trace gases (CO, SO_2 and HCOOH), along with a slight increase in ozone [118]. Other notable examples include the Indonesian fires in October 2015 (supplementary material, figure S8.1, top right) and the Amazon fires in November 2019 (supplementary material, figure S8.1, bottom left), during which TrOC increased by more than 20% over the Maritime Continent and by about 10% over the Amazon and the western South Atlantic, respectively. The 2015 Indonesian fires caused anomalously high CO concentrations [119], which, together with NOx and

Downloaded from royalsocietypublishing.org/rsta/article-pdf/doi/10.1098/rsta.2025.0274/6174218/rsta.2025.0274.pdf
by German Aerospace Centre (DLR) user
on 26 October 2026

volatile organic compounds emissions from the fires, likely enhanced ozone production. The 2019 Amazon fires caused large air quality impacts [120], and previous studies have shown substantial impacts of Amazon biomass burning on regional tropospheric ozone [121]. While the contributions of various processes, such as STE and ENSO, need to be carefully evaluated, these results highlight the substantial potential impacts of wildfires on tropospheric ozone from regional to hemispheric scales.

8. Conclusion

Satellite observations provide a unique and powerful capability for mapping and monitoring changes in tropospheric ozone, with important implications for both air quality and climate [6]. Yet, measuring tropospheric ozone from space remains intrinsically challenging. The relatively weak tropospheric signal must be distinguished from the overlying stratosphere. Multiple complementary retrieval approaches have been developed, each with distinct sources of uncertainties. Additional complications arise from differences in sampling strategies and vertical sensitivities among instruments, which can influence the representation of tropospheric ozone variability. Analyses based on individual datasets are therefore more prone to bias, whereas multi-sensor and multi-record approaches help mitigate such limitations. Nonetheless, substantial challenges persist in resolving ozone variability at fine spatial scales and in producing robust assessments of its long-term evolution.

Substantial progress has been achieved since the challenges listed above were highlighted in the first TOAR assessment in 2018 [16]. The Earth observation community has greatly advanced the number, length, resolution and quality of satellite-based tropospheric ozone datasets. In parallel, new data harmonization approaches have demonstrated their value in reducing the influence of differences in vertical sampling. Building on these advances, this second TOAR assessment introduces robust methods to combine 15 harmonized satellite records and to more comprehensively characterize their associated uncertainties. Overall, we find a markedly improved agreement among satellite datasets compared to TOAR-I, as well as good agreement with ozonesonde and chemical reanalysis data, enabling stronger constraints for all considered ozone metrics. This TOAR-II report evaluates the present-day mean state and seasonal cycle of TrOC (January 2018–December 2022, surface to thermal tropopause), their evolution and trends between 2005 and 2019/2022 and selected episodic events. This present-day period was marked by unique atmospheric conditions following the COVID-19 pandemic and several extreme wildfires that impacted ozone compared to its long-term state.

We estimate the 2018–2022 mean global tropospheric ozone burden at 336.0 ± 6.5 Tg, virtually identical to the TOAR-I estimate for 2010–2014, but with reduced uncertainty and better coverage of the polar regions. Combined satellite data furthermore provide a more finely resolved view than was possible for TOAR-I on the seasonal cycle and regional patterns of ozone, including maxima exceeding 40 DU across highly populated regions such as the IGP, the NCP and the eastern Mediterranean-Middle East. Because column concentrations are influenced by the vertical extent of the troposphere, analyses combining surface and vertical profile observations are required to separate the contributions of near-surface ozone from those of ozone aloft. The enhanced temporal (i.e. monthly) and spatial (i.e. $1° \times 1°$) resolution enables more confident assessment of both mean states and variability.

The combined satellite anomaly time series reveal that tropospheric ozone changes are nonlinear, shaped by a combination of a slowly changing background, interannual variability (e.g. ENSO) and episodic events. During 2005–2019, the strongest increases in tropospheric ozone (>2–3% per decade) were found across a broad region extending from Siberia to the Bay of Bengal and into the North Pacific, but also over western Canada, northern Europe, Brazil and the zonal belt between the Middle East and the Caribbean. Meanwhile, declines are found in most regions after 2020–2021, resulting in an overall net decrease in ozone across two-thirds of the globe with

Downloaded from royalsocietypublishing.org/rsta/article-pdf/doi/10.1098/rsta.2025.0274/6174218/rsta.2025.0274.pdf
by German Aerospace Centre (DLR) user
on 26 October 2026

respect to 2005. The analysis also underscores the role of climate variability and dynamical processes, including ENSO and STE, in modulating TrOC.

The combined satellite data also capture abrupt short-term changes associated with major perturbations. The COVID-19 pandemic led to several years of widespread decreases cumulating to up to 7% in the extratropics, consistent across multiple observing systems. Extreme wildfire events, such as the Indonesian and Australian fires in 2020 and large tropical biomass burning episodes in 2015 and 2019, also produced consistent increases of 10–20% at regional and hemispheric scales. These results highlight the sensitivity of tropospheric ozone to both anthropogenic and natural drivers. At the same time, the assessment underscores the importance of maintaining continued observations in order to monitor potential future increases and evolving variability. Sustained and coordinated satellite measurements, together with continued methodological improvements, remain essential for tracking and mapping changes in tropospheric ozone and for informing policy decisions that support co-benefits for air quality and climate.

Data accessibility. The combined satellite tropospheric ozone data generated and analysed in this study are available at http://doi.org/10.18758/39zdhztg. The individual harmonized satellite records from which this combined dataset was derived are available at [122].

Supplementary material is available online [123].

Declaration of AI use. We have not used AI-assisted technologies in creating this article.

Authors' contributions. D.H.: conceptualization, data curation, formal analysis, investigation, methodology, project administration, resources, software, supervision, validation, visualization, writing—original draft, writing—review and editing; K.M.: conceptualization, formal analysis, funding acquisition, investigation, methodology, project administration, software, supervision, validation, visualization, writing—original draft, writing—review and editing; G.D.: conceptualization, data curation, formal analysis, investigation, methodology, software, validation, visualization, writing—original draft, writing—review and editing; E.A.P.: conceptualization, data curation, formal analysis, investigation, methodology, software, validation, visualization, writing—original draft, writing—review and editing; V.F.S.: conceptualization, data curation, formal analysis, investigation, methodology, software, validation, visualization, writing—original draft, writing—review and editing; C.A.: investigation, writing—review and editing; B.B.: investigation, writing—review and editing; A.B.: investigation, writing—review and editing; M.C.-E.: investigation; J.C.: investigation, writing—review and editing; K.-P.H.: investigation, writing—review and editing; A.K.: investigation, writing—review and editing; N.A.K.: investigation, writing—review and editing; J.-C.L.: funding acquisition, writing—review and editing; D.L.: investigation, writing—review and editing; A.P.O.-C.: investigation, writing—review and editing; R.S.: investigation, writing—review and editing; R.V.M.: investigation, writing—review and editing; J.P.V.: investigation, writing—review and editing; C.W.: investigation, writing—review and editing; J.R.Z.: investigation.

All authors gave final approval for publication and agreed to be held accountable for the work performed therein.

Conflict of interest declaration. We declare we have no competing interests.

Funding. The authors acknowledge guidance and support from the International Global Atmospheric Chemistry (IGAC) project. The Tropospheric Ozone Assessment Report, Phase II (TOAR-II) has been conducted as a sponsored IGAC activity. D.H., A.K. and J.-C.L. were supported by the Royal Belgian Institute for Space Aeronomy (BIRA-IASB) and by the Belgian federal Science Policy Office (BELSPO) through the BRAIN-be 2.0 research project TAPIOWCA (grant B2/223/P1/TAPIOWCA, 2022–2025) and the ProDEx project TROVA-3 (PEA 4000144130, 2024–2025). This work has been supported by the National Aeronautics and Space Administration (NASA). Part of this research was carried out at the Jet Propulsion Laboratory, California Institute of Technology, under contract with the National Aeronautics and Space Administration (80NM0018D0004). We also acknowledge the support of the NASA Atmospheric Composition: Aura Science Team Program (19-AURAST19-0044), Earth Science U.S. Participating Investigator program (22-EUSPI22-0005), ACMAP (22-ACMAP22-0013) and the NASA TROPESS project. IASI is a joint mission of EUMETSAT and the Centre National d'Etudes Spatiales (CNES, France). Part of this project was supported by ESA through the Ozone project in its Climate Change Initiative programme and the OREGANO project (Ozone Recovery from Merged Observational Data and Model Analysis). The French scientists are grateful to CNES and Centre National de la Recherche Scientifique (CNRS) for financial support. We acknowledge the support for the IASI-GOME2 multi-spectral ozone product development, consolidation and production from CNES (via the TOSCA -

Downloaded from royalsocietypublishing.org/rsta/article-pdf/doi/10.1098/rsta.2025.0274/6174218/rsta.2025.0274.pdf
by German Aerospace Centre (DLR) user
on 26 October 2026

Terre Océan Surface Continentale Atmosphère - projects TOTICE 2023-present and SURVEYPOLLUTION 2014-2023), University Paris Est Créteil (UPEC), the AERIS French National Atmospheric Data Centre and Centre National de Recherche Scientifique - Institut National des Scienes de l'Univers (CNRS-INSU, with the Project SYNAEROZON from the Programme National de Télédétection Spatiale). The KNMI contribution to this work was supported by the Netherlands Space Agency under the TROPOMI Science contract.

Acknowledgements. We acknowledge the use of data products from NASA (Aura and EOS Terra and Aqua satellite missions). The authors acknowledge the AERIS data infrastructure for providing access to the IASI-CDR Level 2 ozone data used in this study (http://www.aeris-data.fr), ULB-LATMOS for the development of the retrieval algorithms and EUMETSAT/AC SAF for ozone data production. This work contains modified Copernicus Sentinel-5P data. We wish to acknowledge and express our appreciation for the coordination efforts undertaken by CEOS Atmospheric Composition Virtual Constellation (AC-VC); the collaborative work facilitated through CEOS AC-VC has been instrumental for the validation and harmonization of the tropospheric ozone satellite records. We are very grateful to several TOAR participants Mark Weber, Evgenios Agathokleous, Owen R. Cooper, Debra E. Kollonige and Brian Kerridge who provided valuable comments on a draft manuscript.

References

1. Tarasick D *et al*. 2019 Tropospheric Ozone Assessment Report: tropospheric ozone from 1877 to 2016, observed levels, trends and uncertainties. *Elem.: Sci. Anth.* **7**, 39. (doi:10.1525/elementa.376)
2. Gaudel A *et al*. 2024 Tropical tropospheric ozone distribution and trends from in situ and satellite data. *Atmos. Chem. Phys.* **24**, 9975–10 000. (doi:10.5194/acp-24-9975-2024)
3. Turnock ST, Akritidis D, Horowitz L, Mertens M, Pozzer A, Reddington CL, Wang H, Zhou P, O'Connor F. 2025 Drivers of change in peak-season surface ozone concentrations and impacts on human health over the historical period (1850–2014). *Atmos. Chem. Phys.* **25**, 7111–7136. (doi:10.5194/acp-25-7111-2025)
4. Cook J, Yadav DS, Hayes F, Booth N, Bland S, Pande P, Thankappan S, Emberson L. 2025 Modelling ozone-induced changes in wheat amino acids and protein quality using a process-based crop model. *Biogeosciences* **22**, 1035–1056. (doi:10.5194/bg-22-1035-2025)
5. Chang KL, McDonald BC, Harkins C, Cooper OR. 2025 Surface ozone trend variability across the United States and the impact of heat waves (1990–2023). *Atmos. Chem. Phys.* **25**, 5101–5132. (doi:10.5194/acp-25-5101-2025)
6. Szopa S *et al*. 2026 Tropospheric Ozone Assessment Report II: Ozone interactions with climate change: drivers and long-term trends. *Phil. Trans. R. Soc. A* **384**. (doi:10.1098/rsta.2025.0272)
7. Schultz MG *et al*. 2017 Tropospheric Ozone Assessment Report: database and metrics data of global surface ozone observations. *Elem.: Sci. Anth.* **5**, 58. (doi:10.1525/elementa.244)
8. Van Malderen R *et al*. 2025 Ground-based tropospheric ozone measurements: regional tropospheric ozone column trends from the TOAR-II/HEGIFTOM homogenized datasets. *Atmos. Chem. Phys.* **25**, 9905–9935. (doi:10.5194/acp-25-9905-2025)
9. Wang H, Tarasick DW, Liu J, Smit HGJ, Van Malderen R, Shen L, Blot R, Zhao T. 2024 Consistency evaluation of tropospheric ozone from ozonesonde and IAGOS (In-service Aircraft for a Global Observing System) observations: vertical distribution, ozonesonde types, and station–airport distance. *Atmos. Chem. Phys.* **24**, 11 927–11 942. (doi:10.5194/acp-24-11927-2024)
10. Van Malderen R *et al*. 2025 Global ground-based tropospheric ozone measurements: reference data and individual site trends (2000–2022) from the TOAR-II/HEGIFTOM project. *Atmos. Chem. Phys.* **25**, 7187–7225. (doi:10.5194/acp-25-7187-2025)
11. Young PJ *et al*. 2018 Tropospheric Ozone Assessment Report: assessment of global-scale model performance for global and regional ozone distributions, variability, and trends. *Elem.: Sci. Anth.* **6**, 10. (doi:10.1525/elementa.265)
12. Sekiya T *et al*. 2025 Assessing the relative impacts of satellite ozone and its precursor observations to improve global tropospheric ozone analysis using multiple chemical reanalysis systems. *Atmos. Chem. Phys.* **25**, 2243–2268. (doi:10.5194/acp-25-2243-2025)
13. Inness A *et al*. 2019 The CAMS reanalysis of atmospheric composition. *Atmos. Chem. Phys.* **19**, 3515–3556. (doi:10.5194/acp-19-3515-2019)

Downloaded from royalsocietypublishing.org/rsta/article-pdf/doi/10.1098/rsta.2025.0274/6174218/rsta.2025.0274.pdf
by German Aerospace Centre (DLR) user
on 26 October 2026

14. Hickman SHM *et al*. 2025 Applications of machine learning and artificial intelligence in tropospheric ozone research. *Geosci. Model Dev.* **18**, 8777–8800. (doi:10.5194/gmd-18-8777-2025)
15. Jones D *et al*. 2026 Assessment of regional and interannual variations in tropospheric ozone in chemical reanalyses. *Atmospheric Chemistry and Physics* **26**, 6655–6682. (doi:10.5194/acp-26-6655-2026)
16. Gaudel A *et al*. 2018 Tropospheric Ozone Assessment Report: present-day distribution and trends of tropospheric ozone relevant to climate and global atmospheric chemistry model evaluation. *Elem.: Sci. Anth.* **6**, 39. (doi:10.1525/elementa.291)
17. Coldewey-Egbers M, Loyola R. DG, Latter B, Siddans R, Kerridge B, Hubert D, van Roozendael M, Eisinger M. 2025 The novel GOME-type Ozone Profile Essential Climate Variable (GOP-ECV) data record covering the past 26 years. *Atmos. Meas. Tech.* **18**, 5485–5505. (doi:10.5194/amt-18-5485-2025)
18. Keppens A *et al*. 2025 Harmonisation of sixteen tropospheric ozone satellite data records. *Atmos. Meas. Tech.* **18**, 6893–6916. (doi:10.5194/amt-18-6893-2025)
19. Keppens A *et al*. 2024 5 years of Sentinel-5P TROPOMI operational ozone profiling and geophysical validation using ozonesonde and lidar ground-based networks. *Atmos. Meas. Tech.* **17**, 3969–3993. (doi:10.5194/amt-17-3969-2024)
20. Boynard A *et al*. 2025 Assessment of 16-year tropospheric ozone trends from the IASI Climate Data Record. *Atmos. Chem. Phys.* **25**, 11 719–11 755. (doi:10.5194/acp-25-11719-2025)
21. Clerbaux C *et al*. 2009 Monitoring of atmospheric composition using the thermal infrared IASI/MetOp sounder. *Atmos. Chem. Phys.* **9**, 6041–6054. (doi:10.5194/acp-9-6041-2009)
22. Clerbaux C *et al*. 2015 Tracking pollutants from space: eight years of IASI satellite observation. *Comptes Rendus Géosci.* **347**, 134–144. (doi:10.1016/j.crte.2015.06.001)
23. Dufour G, Eremenko M, Cuesta J, Ancellet G, Gill M, Maillard Barras E, Van Malderen R. 2025 Performance assessment of the IASI-O3 KOPRA product for observing midlatitude tropospheric ozone evolution for 15 years: validation with ozone sondes and consistency of the three IASI instruments. *Atmos. Meas. Tech.* **18**, 5049–5070. (doi:10.5194/amt-18-5049-2025)
24. Cuesta J *et al*. 2013 Satellite observation of lowermost tropospheric ozone by multispectral synergism of IASI thermal infrared and GOME-2 ultraviolet measurements over Europe. *Atmos. Chem. Phys.* **13**, 9675–9693. (doi:10.5194/acp-13-9675-2013)
25. Fu D, Worden JR, Liu X, Kulawik SS, Bowman KW, Natraj V. 2013 Characterization of ozone profiles derived from Aura TES and OMI radiances. *Atmos. Chem. Phys.* **13**, 3445–3462. (doi:10.5194/acp-13-3445-2013)
26. Pennington EA, Osterman GB, Payne VH, Miyazaki K, Bowman KW, Neu JL. 2025 Quantifying biases in TROPESS AIRS, CrIS, and joint AIRS+OMI tropospheric ozone products using ozonesondes. *Atmos. Chem. Phys.* **25**, 8533–8552. (doi:10.5194/acp-25-8533-2025)
27. Fu D *et al*. 2018 Retrievals of tropospheric ozone profiles from the synergism of AIRS and OMI: methodology and validation. *Atmos. Meas. Tech.* **11**, 5587–5605. (doi:10.5194/amt-11-5587-2018)
28. Sofieva VF, Hänninen R, Sofiev M, Szelag M, Lee HS, Tamminen J, Retscher C. 2022 Synergy of using nadir and limb instruments for tropospheric ozone monitoring (SUNLIT). *Atmos. Meas. Tech.* **15**, 3193–3212. (doi:10.5194/amt-15-3193-2022)
29. Arosio C *et al*. 2025 Intercomparison of tropospheric ozone column datasets from combined nadir and limb satellite observations. *Atmos. Meas. Tech.* **18**, 3247–3265. (doi:10.5194/amt-18-3247-2025)
30. Ziemke JR, Chandra S, Duncan BN, Froidevaux L, Bhartia PK, Levelt PF, Waters JW. 2006 Tropospheric ozone determined from Aura OMI and MLS: evaluation of measurements and comparison with the Global Modeling Initiative's Chemical Transport Model. *J. Geophys. Res.* **111**, D19303. (doi:10.1029/2006JD007089)
31. Ziemke JR, Chandra S, Labow GJ, Bhartia PK, Froidevaux L, Witte JC. 2011 A global climatology of tropospheric and stratospheric ozone derived from Aura OMI and MLS measurements. *Atmos. Chem. Phys.* **11**, 9237–9251. (doi:10.5194/acp-11-9237-2011)
32. Orfanoz-Cheuquelaf A, Arosio C, Rozanov A, Weber M, Ladstätter-Weißenmayer A, Burrows JP, Thompson AM, Stauffer RM, Kollonige DE. 2024 Tropospheric ozone column dataset from OMPS-LP/OMPS-NM limb–nadir matching. *Atmos. Meas. Tech.* **17**, 1791–1809. (doi:10.5194/amt-17-1791-2024)

Downloaded from royalsocietypublishing.org/rsta/article-pdf/doi/10.1098/rsta.2025.0274/6174218/rsta.2025.0274.pdf
by German Aerospace Centre (DLR) user
on 26 October 2026

33. Ziemke JR *et al*. 2022 NASA satellite measurements show global-scale reductions in free tropospheric ozone in 2020 and again in 2021 during COVID-19. *Geophys. Res. Lett.* **49**, e2022GL098712. (doi:10.1029/2022GL098712)
34. Marshak A *et al*. 2018 Earth Observations from DSCOVR EPIC Instrument. *Bull. Amer. Meteorol. Soc.* **99**, 1829–1850. (doi:10.1175/BAMS-D-17-0223.1)
35. Gelaro R *et al*. 2017 The modern-era retrospective analysis for research and applications, version 2 (MERRA-2). *J. Climate* **30**, 5419–5454. (doi:10.1175/JCLI-D-16-0758.1)
36. Wargan K, Labow G, Frith S, Pawson S, Livesey N, Partyka G. 2017 Evaluation of the ozone fields in NASA's MERRA-2 reanalysis. *J. Climate* **30**, 2961–2988. (doi:10.1175/JCLI-D-16-0699.1)
37. Kramarova NA, Ziemke JR, Huang LK, Herman JR, Wargan K, Seftor CJ, Labow GJ, Oman LD. 2021 Evaluation of version 3 total and tropospheric ozone columns from earth polychromatic imaging camera on deep space climate observatory for studying regional scale ozone variations. *Front. Remote Sens.* **2**, 734071. (doi:10.3389/frsen.2021.734071)
38. Ziemke JR, Kramarova NA, Frith SM, Huang KL, Baek K, Herman JR. 2025 Ten years of tropospheric ozone from DSCOVR EPIC: science and applications. *Front. Remote Sens.* **6**, 1634922. (doi:10.3389/frsen.2025.1634922)
39. Heue KP, Coldewey-Egbers M, Delcloo A, Lerot C, Loyola D, Valks P, van Roozendael M. 2016 Trends of tropical tropospheric ozone from 20 years of European satellite measurements and perspectives for the Sentinel-5 Precursor. *Atmos. Meas. Tech.* **9**, 5037–5051. (doi:10.5194/amt-9-5037-2016)
40. Fishman J, Larsen JC. 1987 Distribution of total ozone and stratospheric ozone in the tropics: implications for the distribution of tropospheric ozone. *J. Geophys. Res. Atmos.* **92**, 6627–6634. (doi:10.1029/JD092iD06p06627)
41. Ziemke JR, Chandra S, Bhartia PK. 1998 Two new methods for deriving tropospheric column ozone from TOMS measurements: assimilated UARS MLS/HALOE and convective-cloud differential techniques. *J. Geophys. Res.* **103**, 22 115–22 127. (doi:10.1029/98JD01567)
42. Maratt Satheesan S, Eichmann KU, Burrows JP, Weber M, Stauffer R, Thompson AM, Kollonige D. 2024 Improved convective cloud differential (CCD) tropospheric ozone from S5P-TROPOMI satellite data using local cloud fields. *Atmos. Meas. Tech.* **17**, 6459–6484. (doi:10.5194/egusphere-2025-306)
43. Maratt Satheesan S, Eichmann KU, Weber M, Van Malderen R, Stauffer R, Tarasick D. 2025 Extension of the S5P-TROPOMI CCD tropospheric ozone retrieval to mid-latitudes. *EGUsphere*. https://doi.org/10.5194/egusphere-2024-3759.
44. Leventidou E, Weber M, Eichmann KU, Burrows JP, Heue KP, Thompson AM, Johnson BJ. 2018 Harmonisation and trends of 20-year tropical tropospheric ozone data. *Atmos. Chem. Phys.* **18**, 9189–9205. (doi:10.5194/acp-18-9189-2018)
45. Ziemke JR *et al*. 2019 Trends in global tropospheric ozone inferred from a composite record of TOMS/OMI/MLS/OMPS satellite measurements and the MERRA-2 GMI simulation. *Atmos. Chem. Phys.* **19**, 3257–3269. (doi:10.5194/acp-19-3257-2019)
46. Smit HGJ, Thompson AM, ASOPOS 2.0 Panel. 2021 Ozonesonde measurement principles and best operational practices. WMO Global Atmosphere Watch Report Series No. 268. Geneva, Switzerland: World Meteorological Organization (WMO).
47. Miyazaki K *et al*. 2020 Updated tropospheric chemistry reanalysis and emission estimates, TCR-2, for 2005-2018. *Earth Syst. Sci. Data* **12**, 2223–2259. (doi:10.5194/essd-12-2223-2020)
48. Miyazaki K, Marchetti Y, Montgomery J, Lu S, Bowman K. 2025 Identifying drivers of surface ozone bias in global chemical reanalysis with explainable machine learning. *Atmos. Chem. Phys.* **25**, 8507–8532. (doi:10.5194/acp-25-8507-2025)
49. Chang KL, Cooper OR, Gaudel A, Petropavlovskikh I, Effertz P, Morris G, McDonald BC. 2024 Technical note: challenges in detecting free tropospheric ozone trends in a sparsely sampled environment. *Atmos. Chem. Phys.* **24**, 6197–6218. (doi:10.5194/acp-24-6197-2024)
50. Hoffmann L, Spang R. 2022 An assessment of tropopause characteristics of the ERA5 and ERA-interim meteorological reanalyses. *Atmos. Chem. Phys.* **22**, 4019–4046. (doi:10.5194/acp-22-4019-2022)
51. Chang KL, Schultz MG, Lan X, McClure-Begley A, Petropavlovskikh I, Xu X, Ziemke JR. 2021 Trend detection of atmospheric time series: incorporating appropriate uncertainty estimates and handling extreme events. *Elem.: Sci. Anth.* **9**, 00035. (doi:10.1525/elementa.2021.00035)

Downloaded from royalsocietypublishing.org/rsta/article-pdf/doi/10.1098/rsta.2025.0274/6174218/rsta.2025.0274.pdf
by German Aerospace Centre (DLR) user
on 26 October 2026

52. Wespes C, Hurtmans D, Clerbaux C, Coheur PF. 2017 O3 variability in the troposphere as observed by IASI over 2008-2016: contribution of atmospheric chemistry and dynamics. *J. Geophys. Res. Atmos.* **122**, 2429–2451. (doi:10.1002/2016jd025875)
53. Chang KL, Schultz MG, Koren G, Selke N. 2023 Guidance note on best statistical practices for TOAR analyses. (doi:10.48550/arXiv.2304.14236)
54. Keeble J *et al*. 2026 Tropospheric Ozone Assessment Report II: stratosphere-troposphere exchange of ozone. *Phil. Trans. R. Soc. A* **384**. (doi:10.1098/rsta.2025.0271)
55. Chang KL *et al*. 2023 Diverging ozone trends above Western North America: boundary layer decreases versus free tropospheric increases. *J. Geophys. Res. Atmos.* **128**, e2022JD038090. (doi:10.1029/2022JD038090)
56. Froidevaux L, Kinnison DE, Gaubert B, Schwartz MJ, Livesey NJ, Read WG, Bardeen CG, Ziemke JR, Fuller RA. 2025 Tropical upper-tropospheric trends in ozone and carbon monoxide (2005–2020): observational and model results. *Atmos. Chem. Phys.* **25**, 597–624. (doi:10.5194/acp-25-597-2025)
57. Thompson AM *et al*. 2025 Tropical tropospheric ozone trends (1998 to 2023): new perspectives from SHADOZ, IAGOS and OMI/MLS observations. *Atmos. Chem. Phys.* **25**, 18 475–18 507. (doi:10.5194/acp-25-18475-2025)
58. Stauffer RM *et al*. 2024 Dynamical drivers of free-tropospheric ozone increases over equatorial Southeast Asia. *Atmos. Chem. Phys.* **24**, 5221–5234. (doi:10.5194/acp-24-5221-2024)
59. Cochrane D, Orcutt GH. 1949 Application of least squares regression to relationships containing auto-correlated error terms. *J. Amer. Stat. Assoc.* **44**, 32–61. (doi:10.1080/01621459.1949.10483290)
60. Petropavlovskikh I, Godin-Beekmann S, Hubert D, Damadeo R, Hassler B, Sofieva V. 2019 SPARC/IO3C/GAW Report on long-term ozone trends and uncertainties in the stratosphere. SPARC Report No. 9, GAW Report No. 241, WCRP-17/2018. Geneva, Switzerland: World Meteorological Organization (WMO).
61. Cooper OR *et al*. 2014 Global distribution and trends of tropospheric ozone: an observation-based review. *Elem. Sci. Anth.* **2**, 000029. (doi:10.12952/journal.elementa.000029)
62. Elshorbany Y *et al*. 2024 Tropospheric ozone precursors: global and regional distributions, trends, and variability. *Atmos. Chem. Phys.* **24**, 12 225–12 257. (doi:10.5194/acp-24-12225-2024)
63. Monks PS *et al*. 2015 Tropospheric ozone and its precursors from the urban to the global scale from air quality to short-lived climate forcer. *Atmos. Chem. Phys.* **15**, 8889–8973. (doi:10.5194/acp-15-8889-2015)
64. Archibald AT *et al*. 2020 Tropospheric Ozone Assessment Report: a critical review of changes in the tropospheric ozone burden and budget from 1850 to 2100. *Elem.: Sci. Anth.* **8**, 034. (doi:10.1525/elementa.2020.034)
65. Bowman H *et al*. 2022 Changes in anthropogenic precursor emissions drive shifts in the ozone seasonal cycle throughout the northern midlatitude troposphere. *Atmos. Chem. Phys.* **22**, 3507–3524. (doi:10.5194/acp-22-3507-2022)
66. Wang T, Wei XL, Ding AJ, Poon CN, Lam KS, Li YS, Chan LY, Anson M. 2009 Increasing surface ozone concentrations in the background atmosphere of Southern China, 1994-2007. *Atmos. Chem. Phys.* **9**, 6217–6227. (doi:10.5194/acp-9-6217-2009)
67. Dufour G, Eremenko M, Orphal J, Flaud JM. 2010 IASI observations of seasonal and day-to-day variations of tropospheric ozone over three highly populated areas of China: Beijing, Shanghai, and Hong Kong. *Atmos. Chem. Phys.* **10**, 3787–3801. (doi:10.5194/acp-10-3787-2010)
68. Ding AJ, Wang T, Thouret V, Cammas JP, Nédélec P. 2008 Tropospheric ozone climatology over Beijing: analysis of aircraft data from the MOZAIC program. *Atmos. Chem. Phys.* **8**, 1–13. (doi:10.5194/acp-8-1-2008)
69. Li S, Wang T, Huang X, Pu X, Li M, Chen P, Yang XQ, Wang M. 2018 Impact of East Asian summer monsoon on surface ozone pattern in China. *J. Geophys. Res.: Atmos.* **123**, 1401–1411. (doi:10.1002/2017JD027190)
70. Lu X, Zhang L, Liu X, Gao M, Zhao Y, Shao J. 2018 Lower tropospheric ozone over India and its linkage to the South Asian monsoon. *Atmos. Chem. Phys.* **18**, 3101–3118. (doi:10.5194/acp-18-3101-2018)
71. Gong W *et al*. 2025 Modelling Arctic lower-tropospheric ozone: processes controlling seasonal variations. *Atmos. Chem. Phys.* **25**, 8355–8405. (doi:10.5194/acp-25-8355-2025)

Downloaded from royalsocietypublishing.org/rsta/article-pdf/doi/10.1098/rsta.2025.0274/6174218/rsta.2025.0274.pdf
by German Aerospace Centre (DLR) user
on 26 October 2026

72. Scheeren HA *et al*. 2003 The impact of monsoon outflow from India and Southeast Asia in the upper troposphere over the eastern Mediterranean. *Atmos. Chem. Phys.* **3**, 1589–1608. (doi:10.5194/acp-3-1589-2003)
73. Zanis P, Hadjinicolaou P, Pozzer A, Tyrlis E, Dafka S, Mihalopoulos N, Lelieveld J. 2014 Summertime free-tropospheric ozone pool over the eastern Mediterranean/Middle East. *Atmos. Chem. Phys.* **14**, 115–132. (doi:10.5194/acp-14-115-2014)
74. Dayan U, Ricaud P, Zbinden R, Dulac F. 2017 Atmospheric pollution over the eastern Mediterranean during summer—a review. *Atmos. Chem. Phys.* **17**, 13 233–13 263. (doi:10.5194/acp-17-13233-2017)
75. Tyrlis E, Škerlak B, Sprenger M, Wernli H, Zittis G, Lelieveld J. 2014 On the linkage between the Asian summer monsoon and tropopause fold activity over the eastern Mediterranean and the Middle East. *J. Geophys. Res.* **119**, 3202–3221. (doi:10.1002/2013JD021113)
76. Akritidis D, Pozzer A, Zanis P, Tyrlis E, Škerlak B, Sprenger M, Lelieveld J. 2016 On the role of tropopause folds in summertime tropospheric ozone over the eastern Mediterranean and the Middle East. *Atmos. Chem. Phys.* **16**, 14 025–14 039. (doi:10.5194/acp-16-14025-2016)
77. Akritidis D, Pozzer A, Flemming J, Inness A, Zanis P. 2021 A global climatology of tropopause folds in CAMS and MERRA-2 reanalyses. *J. Geophys. Res.: Atmos.* **126**, e2020JD034115. (doi:10.1029/2020JD034115)
78. Owen RC, Cooper OR, Stohl A, Honrath RE. 2006 An analysis of the mechanisms of North American pollutant transport to the central North Atlantic lower free troposphere. *J. Geophys. Res.* **111**, D23S58. (doi:10.1029/2006JD007062)
79. Corral AF *et al*. 2021 An overview of atmospheric features over the Western North Atlantic Ocean and North American East Coast - Part 1: analysis of aerosols, gases, and wet deposition chemistry. *J. Geophys. Res.* **126**, e2020JD032592. (doi:10.1029/2020JD032592)
80. Cuevas E, González Y, Rodríguez S, Guerra JC, Gómez-Peláez AJ, Alonso-Pérez S, Bustos J, Milford C. 2013 Assessment of atmospheric processes driving ozone variations in the subtropical North Atlantic free troposphere. *Atmos. Chem. Phys.* **13**, 1973–1998. (doi:10.5194/acp-13-1973-2013)
81. Cooper OR *et al*. 2020 Multi-decadal surface ozone trends at globally distributed remote locations. *Elem.: Sci. Anth.* **8**, 23. (doi:10.1525/elementa.420)
82. Sauvage B, Martin RV, van Donkelaar A, Ziemke JR. 2007 Quantification of the factors controlling tropical tropospheric ozone and the South Atlantic maximum. *J. Geophys. Res.* **112**, D11309. (doi:10.1029/2006JD008008)
83. Okamoto S, Cuesta J, Dufour G, Eremenko M, Miyazaki K, Boonne C, Tanimoto H, Peischl J, Thompson C. 2026 Natural and anthropogenic influence on tropospheric ozone variability over the tropical Atlantic unveiled by satellite, reanalyses and in situ observations. *Atmos. Chem. Phys.* **26**, 4685–4709. (doi:10.5194/acp-26-4685-2026)
84. Thompson AM, Pickering KE, McNamara DP, Schoeberl MR, Hudson RD, Kim JH, Browell EV, Kirchhoff VWJH, Nganga D. 1996 Where did tropospheric ozone over southern Africa and the tropical Atlantic come from in October 1992? Insights from TOMS, GTE TRACE A, and SAFARI 1992. *J. Geophys. Res.: Atmos.* **101**, 24 251–24 278. (doi:10.1029/96JD01463)
85. Oltmans SJ *et al*. 2013 Recent tropospheric ozone changes—a pattern dominated by slow or no growth. *Atmos. Environ.* **67**, 331–351. (doi:10.1016/j.atmosenv.2012.10.057)
86. Keil M, Jackson DR, Hort MC. 2007 The January 2006 low ozone event over the UK. *Atmos. Chem. Phys.* **7**, 961–972. (doi:10.5194/acp-7-961-2007)
87. Verstraeten WW, Neu JL, Williams JE, Bowman KW, Worden JR, Boersma KF. 2015 Rapid increases in tropospheric ozone production and export from China. *Nat. Geosci.* **8**, 690–695. (doi:10.1038/ngeo2493)
88. Zhang Y, Tao M, Zhang J, Liu Y, Chen H, Cai Z, Konopka P. 2020 Long-term variations in ozone levels in the troposphere and lower stratosphere over Beijing: observations and model simulations. *Atmos. Chem. Phys.* **20**, 13 343–13 354. (doi:10.5194/acp-20-13343-2020)
89. Wang W *et al*. 2022 Long-term trend of ozone pollution in China during 2014–2020: distinct seasonal and spatial characteristics and ozone sensitivity. *Atmos. Chem. Phys.* **22**, 8935–8949. (doi:10.5194/acp-22-8935-2022)
90. Liu Y *et al*. 2023 Drivers of increasing ozone during the two phases of clean air actions in China 2013–2020. *Environ. Sci. Technol.* **57**, 8954–8964. (doi:10.1021/acs.est.3c00054)

Downloaded from royalsocietypublishing.org/rsta/article-pdf/doi/10.1098/rsta.2025.0274/6174218/rsta.2025.0274.pdf
by German Aerospace Centre (DLR) user
on 26 October 2026

91. Rathore A, Gopikrishnan G, Kuttippurath J. 2023 Changes in tropospheric ozone over India: variability, long-term trends and climate forcing. *Atmos. Environ.* **309**, 119959. (doi:10.1016/j.atmosenv.2023.119959)
92. Gao M *et al*. 2020 Ozone pollution over China and India: seasonality and sources. *Atmos. Chem. Phys.* **20**, 4399–4414. (doi:10.5194/acp-20-4399-2020)
93. Chandra S, Ziemke JR, Duncan BN, Diehl TL, Livesey NJ, Froidevaux L. 2009 Effects of the 2006 El Niño on tropospheric ozone and carbon monoxide: implications for dynamics and biomass burning. *Atmos. Chem. Phys.* **9**, 4239–4249. (doi:10.5194/acp-9-4239-2009)
94. Oman LD, Ziemke JR, Douglass AR, Waugh DW, Lang C, Rodriguez JM, Nielsen JE. 2011 The response of tropical tropospheric ozone to ENSO. *Geophys. Res. Lett.* **38**, L13706. (doi:10.1029/2011GL047865)
95. Bruckner M, Pierce RB, Lenzen A. 2024 Examining ENSO-related variability in tropical tropospheric ozone in the RAQMS-Aura chemical reanalysis. *Atmos. Chem. Phys.* **24**, 10 921–10 945. (doi:10.5194/acp-24-10921-2024)
96. Grosvenor MJ, Ardiyani V, Wooster MJ, Gillott S, Green DC, Lestari P, Suri W. 2024 Catastrophic impact of extreme 2019 Indonesian peatland fires on urban air quality and health. *Commun. Earth Environ.* **5**, 649. (doi:10.1038/s43247-024-01813-w)
97. Wainwright CM, Finney DL, Kilavi M, Black E, Marsham JH. 2021 Extreme rainfall in East Africa, October 2019–January 2020 and context under future climate change. *Weather* **76**, 26–31. (doi:10.1002/wea.3824)
98. Pouyaei A, Ginoux P, Naik V, Feng J, Horowitz LW, Paulot F. 2025 ENSO-driven variability in ozone sources and its impact on tropospheric ozone radiative forcing. *Geophys. Res. Lett.* **52**, e2025GL115898. (doi:10.1029/2025GL115898)
99. Seguel RJ *et al*. 2025 Hemispheric differences in ozone across the stratosphere–troposphere exchange region. *Atmos. Chem. Phys.* **25**, 8553–8573. (doi:10.5194/acp-25-8553-2025)
100. Solomon S *et al*. 2022 On the stratospheric chemistry of midlatitude wildfire smoke. *Proc. Natl Acad. Sci. USA* **119**, e2117325119. (doi:10.1073/pnas.2117325119)
101. Zhang S, Solomon S, Zhang J, Kinnison D. 2025 Record-high ozone in the Austral mid-latitude tropopause region driven by dynamical and chemical effects of the 2019 sudden stratospheric warming. *Geophys. Res. Lett.* **52**, e2025GL115588. (doi:10.1029/2025GL115588)
102. Yook S, Thompson DWJ, Solomon S. 2022 Climate impacts and potential drivers of the unprecedented antarctic ozone holes of 2020 and 2021. *Geophys. Res. Lett.* **49**, e2022GL098064. (doi:10.1029/2022GL098064)
103. Gupta AK, Mittal T, Fauria KE, Bennartz R, Kok JF. 2025 The January 2022 Hunga eruption cooled the southern hemisphere in 2022 and 2023. *Commun. Earth Environ.* **6**, 240. (doi:10.1038/s43247-025-02181-9)
104. Yook S, Solomon S, Wang X. 2025 The impact of 2022 Hunga Tonga-Hunga Ha'apai (Hunga) eruption on stratospheric circulation and climate. *J. Geophys. Res.: Atmos.* **130**, e2024JD042943. (doi:10.1029/2024JD042943)
105. Lu X *et al*. 2025 Tropospheric ozone trends and attributions over East and Southeast Asia in 1995–2019: an integrated assessment using statistical methods, machine learning models, and multiple chemical transport models. *Atmos. Chem. Phys.* **25**, 7991–8028. (doi:10.5194/acp-25-7991-2025)
106. Pimlott MA, Pope RJ, Kerridge BJ, Siddans R, Latter BG, Feng W, Chipperfield MP. 2025 Long-term satellite trends of European lower-tropospheric ozone from 1996–2017. *Atmos. Chem. Phys.* **25**, 15 991–16 007. (doi:10.5194/acp-25-15991-2025)
107. Pope RJ *et al*. 2023 Investigation of spatial and temporal variability in lower tropospheric ozone from RAL space UV–Vis satellite products. *Atmos. Chem. Phys.* **23**, 14 933–14 947. (doi:10.5194/acp-23-14933-2023)
108. Pope RJ *et al*. 2024 Investigation of the impact of satellite vertical sensitivity on long-term retrieved lower-tropospheric ozone trends. *Atmos. Chem. Phys.* **24**, 9177–9195. (doi:10.5194/acp-24-9177-2024)
109. Zhang Y, Cooper OR, Gaudel A, Thompson AM, Nédélec P, Ogino SY, West JJ. 2016 Tropospheric ozone change from 1980 to 2010 dominated by equatorward redistribution of emissions. *Nat. Geosci.* **9**, 875–879. (doi:10.1038/ngeo2827)

Downloaded from royalsocietypublishing.org/rsta/article-pdf/doi/10.1098/rsta.2025.0274/6174218/rsta.2025.0274.pdf
by German Aerospace Centre (DLR) user
on 26 October 2026

110. Gaudel A *et al*. 2020 Aircraft observations since the 1990s reveal increases of tropospheric ozone at multiple locations across the Northern Hemisphere. *Sci. Adv.* **6**, eaba8272. (doi:10.1126/sciadv.aba8272)
111. Wang H *et al*. 2022 Global tropospheric ozone trends, attributions, and radiative impacts in 1995–2017: an integrated analysis using aircraft (IAGOS) observations, ozonesonde, and multi-decadal chemical model simulations. *Atmos. Chem. Phys.* **22**, 13 753–13 782. (doi:10.5194/acp-22-13753-2022)
112. Nalam A, Lupaşcu A, Ansari T, Butler T. 2025 Regional and sectoral contributions of NO_x and reactive carbon emission sources to global trends in tropospheric ozone during the 2000–2018 period. *Atmos. Chem. Phys.* **25**, 5287–5311. (doi:10.5194/acp-25-5287-2025)
113. Souri AH *et al*. 2025 Feasibility of robust estimates of ozone production rates using a synergy of satellite observations, ground-based remote sensing, and models. *Atmos. Chem. Phys.* **25**, 2061–2086. (doi:10.5194/acp-25-2061-2025)
114. Pimlott MA, Pope RJ, Kerridge BJ, Siddans R, Latter BG, Ventress LJ, Feng W, Chipperfield MP. 2025 Large reductions in satellite-derived and modelled European lower-tropospheric ozone during and after the COVID-19 pandemic (2020–2022). *Atmos. Chem. Phys.* **25**, 4391–4401. (doi:10.5194/acp-25-4391-2025)
115. Chang KL *et al*. 2022 Impact of the COVID-19 economic downturn on tropospheric ozone trends: an uncertainty weighted data synthesis for quantifying regional anomalies above Western North America and Europe. *AGU Adv.* **3**, e2021AV000542. (doi:10.1029/2021AV000542)
116. Steinbrecht W. 2021 COVID-19 crisis reduces free tropospheric ozone across the Northern Hemisphere. *Geophys. Res. Lett.* **48**, e2020GL091987. (doi:10.1029/2020GL091987)
117. Miyazaki K, Bowman K, Sekiya T, Takigawa M, Neu JL, Sudo K, Osterman G, Eskes H. 2021 Global tropospheric ozone responses to reduced NO_x emissions linked to the COVID-19 worldwide lockdowns. *Sci. Adv.* **7**, eabf7460. (doi:10.1126/sciadv.abf7460)
118. Zhang J, Sheng Z, He Y, Zuo X, Jin B, He M. 2021 Analysis of the impact of the 2019–20 Australian bushfire season on the atmospheric environment. *Front. Earth Sci.* **9,** 566891. (doi:10.3389/feart.2021.566891)
119. Park M, Worden HM, Kinnison DE, Gaubert B, Tilmes S, Emmons LK, Santee ML, Froidevaux L, Boone CD. 2021 Fate of pollution emitted during the 2015 Indonesian fire season. *J. Geophys. Res.: Atmos.* **126**, e2020JD033474. (doi:10.1029/2020JD033474)
120. Butt EW, Conibear L, Knote C, Spracklen DV. 2021 Large air quality and public health impacts due to Amazonian deforestation fires in 2019. *GeoHealth* **5**, e2021GH000429. (doi:10.1029/2021GH000429)
121. Pope RJ *et al*. 2020 Substantial increases in Eastern Amazon and Cerrado biomass burning-sourced tropospheric ozone. *Geophys. Res. Lett.* **47**, e2019GL084143. (doi:10.1029/2019GL084143)
122. Keppens A, Hubert D, Granville J, Lambert J-C. 2025 Harmonised satellite tropospheric ozone Climate Data Records (TAPIOWCA) (Version 1) [Data set]. *BIRA-IASB* (doi:10.18758/r7u4z0he)
123. Hubert D *et al*. 2026 Supplementary material from: Tropospheric Ozone Assessment Report II: Past and present tropospheric ozone using satellite observations. Figshare. (doi:10.6084/m9.figshare.c.8658250)

Downloaded from royalsocietypublishing.org/rsta/article-pdf/doi/10.1098/rsta.2025.0274/6174218/rsta.2025.0274.pdf
by German Aerospace Centre (DLR) user
on 26 October 2026